DISCLAIMER

NATIONAL ENERGY TECHNOLOGY LABORATORY

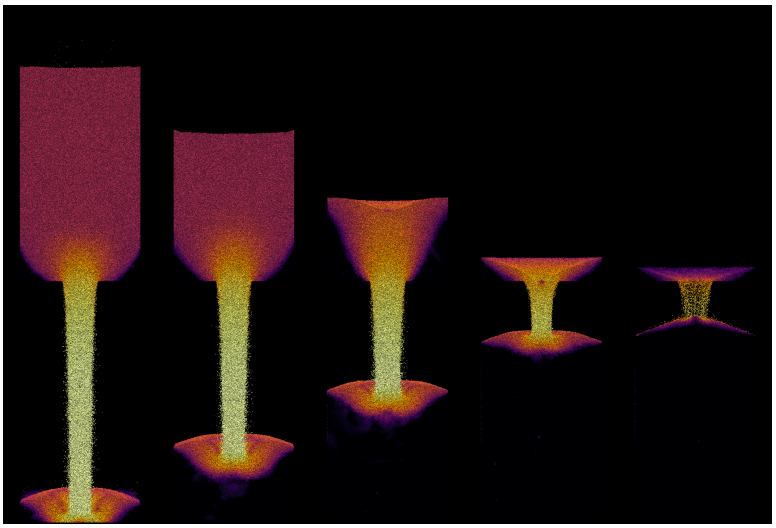

Dense granular flows with MFIX-Exa

March, 2025

U.S. DEPARTMENT OF ENERGY | NATIONAL ENERGY TECHNOLOGY LABORATORY

Office of Fossil Energy and Carbon Management
DOE/NETL-2025/4916

Disclaimer

Cover Illustration:
Discharge of a flat-bottom hopper (with diameter of 5 cm and an opening of 1.5 cm) into a reservoir, particles are colored by the logarithm of their velocity magnitude (ranging from -3 [black] to 0 [white]), only particles in the "back half" ($z \leq 0$) are visualized.

Keywords:
MFIX-Exa, AMReX, DEM, granular

Suggested Citation:
Fullmer, W.D., Rangarajan, D., & Musser, J. (2025). *Dense granular flows with MFIX-Exa*; DOE/NETL-2025/4916, NETL Technical Report Series. U.S. Department of Energy, National Energy Technology Laboratory, Morgantown, WV.

An electronic version of this report can be found at:
`https://netl.doe.gov/energy-analysis/search`

Dense granular flows with MFIX-Exa

William D. Fullmer[1], Deepak Ragarajan[1,2], and Jordan Musser[1]

[1]**National Energy Technology Laboratory, Morgantown, WV 26505**
[2]**NETL Support Contractor, Morgantown, WV 26505**

DOE/NETL-2025/4916

March, 2025

NETL Contacts:

Jordan Musser, Principal Investigator

MaryAnn Clarke, Technical Portfolio Lead

Bryan Morreale, Associate Laboratory Director for Research & Innovation

This page intentionally left blank.

Table of Contents

List of Figures

List of Tables

Executive Summary

This report extends the linear spring dashpot collision model the discrete element method available in MFIX-Exa to include static a static tangential friction force. Additionally, two rolling friction models frequently used in the literature are also implemented. The governing equations are provided with an emphasis on the new terms. The new model is validated by comparison to existing experimental data of single particle oblique collisions. The model is then tested on three dense granular flow problems: the formation of static piles, the discharge from a flat-bottom hopper and the self-induced granular Rayleigh-Taylor instability.

Chapter 1: Introduction

MFIX-Exa (`https://mfix.netl.doe.gov/mfix-exa`) is a recently released multiphase computational fluid dynamics (CFD) code for the simulation of particle-laden gas-solid flows. There are two primary modeling options for the solids phase: discrete element method (DEM) or particle-in-cell (PIC). Whether using high-fidelity DEM, which models individual particles, or low-fidelity PIC, which models statistical elements, MFIX-Exa was developed for performance portability by using the AMReX software framework (`https://github.com/AMReX-Codes/amrex`) which provides the iterators, parallel communication routines, and other tools to support highly efficient operations on structured grid and particle data [6, 7]. To date, the code has been scaled out to at least 512 GPUs on ALCF's Aurora and Polaris, NERSC's Perlmutter and OLCF's Frontier and Summit leadership computers.

MFIX-Exa was originally developed as part of the joint DOE Office of Science and NNSA Exascale Computing Project (ECP) as an Energy Application code [8, 9]. Each ECP application code had an associated challenge problem that was used as a benchmark to demonstrate exascale capabilities. For MFIX-Exa, the challenge problem was a (very short time duration) simulation of NETL's pilot-scale 50kW chemical looping reactor (CLR) [10] with the CFD-DEM method. While the challenge problem helped drive and focus code development, it also drove decisions which narrowed the scope of the resulting code, i.e., the goal was not to develop a general purpose replacement for the MFiX code (`https://mfix.netl.doe.gov/mfix`), but, rather, a performant code possible of simulating the basic physics of the CLR on Frontier or Aurora. (OLCF's Frontier, as it turned out.)

After the challenge problem was satisfied and ECP began to sunset, MFIX-Exa was released publicly and began a new chapter as NETL supported software. As such, the code base is begining to increase in modeling capabilities targeting wider use cases and a wider user base. In this work, we consider the simplified form of tangential friction in the DEM collision model. In MFIX-Exa, only the dynamic tangential force, i.e., Coulomb friction, is applied [11]. The code footprint is reduced by neglecting the static force because the tangential overlap, a neighbor-dependent history (time integrated) term, does not need to be calculated and stored for each colliding pair. This approximation is generally acceptable for multiphase flows [12]–as in the CLR–because the interfacial forces, i.e., drag, typically dictate solids behavior. This is not the case, however, for dense granular flows where solids behavior is dicated entirely particle collisions (or primarily if a gas-phase is included). The details of the simplified and full tangential force within the DEM model are provided in the following section. Additionally, two simple rolling friction models are implemented which may be relevant in some scenarios. Following sections provide validation results and case studies highlighting the improvement of MFIX-Exa DEM to model dense granular flows.

Chapter 2: Discrete Element Method

2.1 Governing Equations

The DEM models individual particles with Newtonian mechanics. The equations governing the position, $\boldsymbol{x}_i$, linear velocity, $\boldsymbol{u}_i$, and angular velocity, $\boldsymbol{\omega}_i$, of a given particle i are,

$$\frac{d\boldsymbol{x}_i}{dt} = \boldsymbol{u}_i \,, \tag{1}$$

$$\frac{dm_i\boldsymbol{u}_i}{dt} = m_i\boldsymbol{g} + \boldsymbol{f}_{iw} + \sum_{j=1}^{N_i^{(c)}} \boldsymbol{f}_{ij} \,, \tag{2}$$

and

$$\frac{dI_i\boldsymbol{\omega}_i}{dt} = \boldsymbol{\tau}_{iw} + \sum_{j=1}^{N_i^{(c)}} \boldsymbol{\tau}_{ij} \,, \tag{3}$$

respectively, where m_i and I_i are the mass and moment of inertia of particle i. Currently in MFIX-Exa, all particles assumed to be spherical so $m_i \equiv \pi\rho_i d_i^3/6$ and $I_i \equiv m_i d_i^2/10$ where ρ_i and d_i are the density and diameter of the i^{th} particle. In this work we assume that the particle properties are constant in time, i.e.,

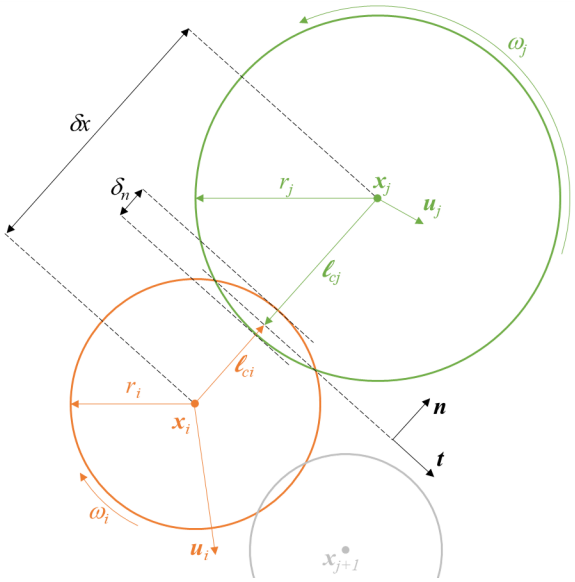

Figure 1: Sketch particles i and j showing collision parameters. Note that only a 2-D projection is shown and that the overlap between the particles has been exaggerated for clarity.

non-reacting, so that m_i and I_i can be brought outside of the time derivatives. The force and torque due to contact between particle i and the wall is represented by $\boldsymbol{f}_{iw}$ and $\boldsymbol{\tau}_{iw}$, respectively. Similarly, the contact force and torque between the particle i and particle j are given by $\boldsymbol{f}_{ij}$ and $\boldsymbol{\tau}_{ij}$ for all j particles in $N_i^{(c)}$, i.e., the set of neighboring particles that are in contact particle i. We also note that, in general, there is also a term $\boldsymbol{f}_{gi}$ in Eq. (2) which is due to the gas-phase acting on particle i, i.e., the interfacial force. This term is dropped because only granular flows are considered herein.

2.2 Collision Model

There are a variety of soft-sphere collision models available in literature [13, 14], with linear spring-dashpot (LSD) [15] and Hertzian [16] varieties being the most commonly applied models for fluidization [17, 18]. MFIX-Exa uses the simpler LSD model originally owing to Cundall and Strack [15]. The essence of the LSD model is that contact forces can be described by a conservative spring and a dissipative dashpot or damper. The collision model is detailed below for particle-particle contacts, which particle-wall contacts are a simplification of, as highlighted in Sec. 2.4.

As shown in Fig. 1, particle i is located at $\boldsymbol{x}_i$, particle j is located at $\boldsymbol{x}_j$ and the position of particle j relative to particle i is $\boldsymbol{x}_{ji} = \boldsymbol{x}_j - \boldsymbol{x}_i$. The two particles are determined to be in contact if the (normal) overlap is positive, i.e., $\delta_n > 0$, where

$$\delta_n = r_i + r_j - \delta x \,, \tag{4}$$

$r_i = d_i/2$ and $r_j = d_j/2$ are the particle radii, and $\delta x = |\boldsymbol{x}_{ji}|$ is the distance between the particles. The unit normal,

$$\boldsymbol{n} = \boldsymbol{x}_{ji}/\delta x \,. \tag{5}$$

The distance to the contact plane from the centers of particles i and j is

$$\ell_{ci} = \frac{\delta x^2 + r_i^2 - r_j^2}{2\delta x} \quad \text{and} \quad \ell_{cj} = \frac{\delta x^2 + r_j^2 - r_i^2}{2\delta x} \,, \tag{6}$$

respectively. Equivalently, we could write $\ell_{cj} = \delta x - \ell_{ci}$ or vice versa. The total relative velocity, i.e., linear and rotational, at the contact surface is

$$\begin{aligned} \boldsymbol{u}_{ij} &= \boldsymbol{u}_i + \ell_{ci}\boldsymbol{n} \times \boldsymbol{\omega}_i - (\boldsymbol{u}_j + \ell_{cj}(-\boldsymbol{n}) \times \boldsymbol{\omega}_j) \\ &= \boldsymbol{u}_i - \boldsymbol{u}_j + (\ell_{ci}\boldsymbol{\omega}_i + \ell_{cj}\boldsymbol{\omega}_j) \times \boldsymbol{n} \,. \end{aligned} \tag{7}$$

The normal and tangential components of the relative velocity are,

$$\boldsymbol{u}_{ij}^{(n)} = (\boldsymbol{u}_{ij} \cdot \boldsymbol{n})\,\boldsymbol{n} \quad \text{and} \quad \boldsymbol{u}_{ij}^{(t)} = \boldsymbol{u}_{ij} - \boldsymbol{u}_{ij}^{(n)}\,, \tag{8}$$

respectively.

The contact force acting on particle i from particle j is decomposed into normal and tangential components,

$$\boldsymbol{f}_{ij}^{(n)} = \boldsymbol{f}_{ij}^{(n)} + \boldsymbol{f}_{ij}^{(t)}\,.$$

The normal force, when in contact ($\delta_n > 0$), is given by,

$$\boldsymbol{f}_{ij}^{(n)} = -k_n \delta_n \boldsymbol{n} - \eta_n \boldsymbol{u}_{ji}^{(n)}\,, \tag{9}$$

where k_n and η_n are the normal spring stiffness and dashpot coefficients, respectively. In MFIX-Exa, these modeling parameters are assumed to be constant for all particles. Likewise, the tangential force is given by

$$\boldsymbol{f}_{ij}^{(t)} = -k_t \boldsymbol{\delta}_t - \eta_n \boldsymbol{u}_{ji}^{(t)}\,, \tag{10}$$

where k_t and η_n are the tangential spring stiffness and dashpot coefficients, respectively. Although the LSD form of the tangential force of Eq. (10) is exactly the same as the normal force in Eq. (9), a very important difference is concealed in the overlap. In the normal direction, the overlap can be computed from the instantaneous information of particle i and particle j. And the displacement vector is simply $\boldsymbol{\delta}_n = \delta_n \boldsymbol{n}$. In the tangential direction, the displacement must be calculated by integrating the relative tangential velocity, Eq. (8), as [19, 20, 21],

$$\boldsymbol{\delta}_t = \int_{t_0}^{t} \boldsymbol{u}_{ij}^{(t)}\, dt\,. \tag{11}$$

where t_0 denotes the first time step for which collision between particles i and j is detected, $\delta_n > 0$. The tangential displacement is a "history" term which must be stored because it can not be calculated from instantaneous particle data. Although not particularly computationally taxing, this can present a non-negligible increase in the memory footprint of the code because this array must be allocated for each particle for each colliding neighbor. In the current implementation, we have set the maximum number of colliding partners to ten. If $N_i^{(c)} > 10$ at any time step for any particle, the code throws an error and terminates. Further, because the frame of reference of the contact plane may rotate during a collision, the tangential displacement may need to be adjusted to remain perpendicular to the normal vector, $\boldsymbol{n}$, i.e., projected onto the tangential plane. David [19] and van der Hoef et al. [22] provide alternative methods for this correction. We have followed the simpler method of David [19],

$$\boldsymbol{\delta}_t = \boldsymbol{\delta}_t' - (\boldsymbol{\delta}_t' \cdot \boldsymbol{n})\,\boldsymbol{n}\,,$$

where $\boldsymbol{\delta}_t'$ is the tangential displacement from the previous iteration. Lastly, the tangential force must be limited by the Coulomb condition,

$$\left|\boldsymbol{f}_{ij}^{(t)}\right| \le \mu_{pp} \left|\boldsymbol{f}_{ij}^{(n)}\right|\,, \tag{12}$$

where μ_{pp} is the particle-particle friction coefficient. Currently, MFIX-Exa only supports two friction coefficients, μ_{pp} for particle-particle collisions and μ_{pw} particle-wall collisions. We note that, technically, μ in Eq. (12) should be a *static* friction coefficient to determine the onset of sliding and a dynamic friction coefficient after sliding begins. However, only a single value is used here because the two coefficients are typically similar and rarely differentiated (if either is even measured at all) in experimental works. The static force in Eq. (10) and the Coulomb limit in Eq. (12) can be combined in two ways. The first, and most obvious way, is to limit the tangential force [15, 20],

$$\boldsymbol{f}_{ij}^{(t)} = \min\left(-k_t \boldsymbol{\delta}_t - \eta_n \boldsymbol{u}_{ji}^{(t)},\ -\mu_{pp}\left|\boldsymbol{f}_{ij}^{(n)}\right| \boldsymbol{t}\right)\,,$$

where $\boldsymbol{t}$ is the tangent direction, discussed below. The second method instead limits the tangential displacement so that the Coulomb limit of Eq. (12) is never exceeded,

$$\boldsymbol{\delta}_t \le \left(\mu_{pp}\left|\boldsymbol{f}_{ij}^{(n)}\right| \boldsymbol{t} - \eta_n \boldsymbol{u}_{ji}^{(t)}\right)/k_t\,. \tag{13}$$

Here, we chose to limit the tangential overlap which is recommended in some previous works [23, 24, 21]. Again, $\boldsymbol{t}$ in Eq. (13) is the tangent direction, which has some ambiguity. The obvious choices for the tangent direction are

1. the direction of the tangential overlap, $\boldsymbol{t} = \boldsymbol{\delta}_t / |\boldsymbol{\delta}_t|$,
2. the direction of the tangential relative velocity, $\boldsymbol{t} = \boldsymbol{u}_{ij}^{(t)} / \left|\boldsymbol{u}_{ij}^{(t)}\right|$, or
3. some combination of the two, chiefly the linear in Eq. (10), $\boldsymbol{t} = \boldsymbol{f}_{ij}^{(t)} / \left|\boldsymbol{f}_{ij}^{(t)}\right|$.

We note that MFiX uses option (1) while the current develop branch of MFIX-Exa uses option (2). Following David et al. [19], we apply option (3) because it makes the direction of the tangential force continuous as the Coulomb limit is exceeded. Additionally, option (3) eliminates the need for some logic to avoid floating point exceptions (divide by zero) in the numerical implementation.

The torque is decomposed into two components,

$$\boldsymbol{\tau}_{ij} = \boldsymbol{\tau}_{ij}^{(c)} + \boldsymbol{\tau}_{ij}^{(r)} ,$$

due to the tangential force from contact and rolling friction, respectively. The contact torque is given by,

$$\boldsymbol{\tau}_{ij}^{(c)} = \ell_{ci} \boldsymbol{n} \times \boldsymbol{f}_{ij}^{(t)} . \tag{14}$$

Torque due to rolling friction is not currently modeled in MFIX-Exa. Two different types of models are considered here. Following Zhou et al. [4], Ai [25], Wensrich and Katterfeld [26], Blais et al. [21], and others, the two types of rolling friction considered are labeled `Model A` and `Model B`. `Model A` rolling friction is given by

$$\boldsymbol{\tau}_{ij}^{(r)} = -\mu_r \hat{r}_{ij} \left| f_{ij}^{(n)} \right| \frac{\boldsymbol{\omega}_{ij}}{|\boldsymbol{\omega}_{ij}|} , \tag{15}$$

where μ_r is a coefficient of rolling friction, $\hat{r}_{ij} = r_i r_j / (r_i + r_j)$ is the harmonic mean of the radii of particles i and j, and $\boldsymbol{\omega}_{ij} = \boldsymbol{\omega}_i - \boldsymbol{\omega}_j$ is the relative angular velocity of particle i relative to the angular velocity of particle j. `Model B` rolling friction is given by

$$\boldsymbol{\tau}_{ij}^{(r)} = -\mu_r \hat{r}_{ij} \left| f_{ij}^{(n)} \right| \boldsymbol{u}_{ij}^{(\omega)} , \tag{16}$$

where $\boldsymbol{u}_{ij}^{(\omega)} = r_i \boldsymbol{\omega}_i - r_j \boldsymbol{\omega}_j$ is the rotational velocity of particle i relative to particle j in the direction of the relative angular velocity difference, $\boldsymbol{\omega}_{ij}$. Technically, the velocity at the contact plane should use ℓ_{ci} and ℓ_{cj} instead of r_i and r_j, respectively. We stick with the approximate version here for consistency with previous works. Additionally, because there is so much uncertainty in modeling this term, the difference between ℓ_{ci} and r_i is negligible by comparison.

Note that there are two differences between these two rolling friction models of Eq. (15) and Eq. (16). The first is the use of $\boldsymbol{\omega}_{ij}$ versus $\boldsymbol{u}_{ij}^{(\omega)}$. The second is that `Model A` only uses $\boldsymbol{\omega}_{ij}$ to determine the unit normal, while in `Model B` $\boldsymbol{\tau}_{ij}^{(r)}$ linearly depends on $\boldsymbol{u}_{ij}^{(\omega)}$. Each of these models have an obvious shortcoming. Because `Model A` does not depend on the angular velocity, it does not vanish in a static assembly. For example, normal forces encountered in a static pile will induce a torque through rolling friction even when the pile is at rest for very long times. `Model B` fixes this issue, now, however, the rolling friction coefficient must have units of inverse velocity, $\left[\mu_r^{(\mathtt{B})}\right] = \mathrm{s/m}$. Of course there is a third modeling option [27], `Model C`, which use a spring and dashpot with a Coulomb-type limiter very analogous to the tangential friction model [25, 21]. This modeling approach can be extended further to include an additional torque term due to twisting resistance. Each additional modeling capability requiring closures which are increasingly difficult to measure experimentally. The current approach is to pursue only options `Model A` and `Model B`, flawed as they are. If the detailed granular modeling offered by including history terms for rolling and twisting torques is needed, it may be best to consider a different code, such as LAMMPS `https://www.lammps.org`.

The models that were neglected in the "current," released version of MFIX-Exa, denoted here as `develop`, were added in a branch, `tangential_history`, on D.R.'s fork. At the time of this writing, these code modifications exist as merge request `!1245` on the main repository. In the following sections, we will see how the inclusion of the static tangential force (i.e., the history term) and rolling friction model(s) play a crucial role in the modeling of dense granular flows.

2.3 Modeling Approach

To close the linear collision model outlined in Sec. 2.2 one must specify at least five unknowns: k_n, η_n, k_t, η_t, μ_{pp}, and a sixth, μ_r, if rolling friction is considered. In MFIX-Exa, k_n, k_t, μ_{pp} and μ_r are scalars, i.e., they take only a single value for all particles. However, the dashpot coefficients are specified on basis of a solids phase or type, referring to a collection of particles. In the equations below, we again consider an i-j collision with particle i belonging to solid phase p and particle j belonging to solid phase q, The normal dashpot coefficient, η_n, is related to the coefficient of restitution [28] by

$$e_{pq} = \exp\left(-\frac{\eta_{n,pq}\delta t_{pq}^{(c)}}{2\hat{m}_{pq}}\right). \tag{17}$$

The effective mass (harmonic mean) is,

$$\hat{m}_{pq} = \frac{\bar{m}_q \bar{m}_q}{\bar{m}_p + \bar{m}_q}$$

where $\bar{m}_p$ and $\bar{m}_q$ is the arithmetic mean of all particles of types p and q, respectively. The (normal) collision duration, $\delta t_{pq}^{(c)}$, is related to the spring constant by

$$\delta t_{pq}^{(c)} = \pi\left[\frac{k_n}{\hat{m}_{pq}} - \left(\frac{\eta_{n,pq}}{2\hat{m}_{pq}}\right)\right]^{-1/2}, \tag{18}$$

Because the restitution coefficient is an easily measurable property, it is more physically intuitive to rearrange Eqs. (17) and (18) as,

$$\eta_{n,pq} = \frac{-2\sqrt{\hat{m}_{ij}k_n}\,|\ln e_{pq}|}{\sqrt{\pi^2 + \ln^2 e_{pq}}}. \tag{19}$$

The restitution coefficient must be provided as an upper triangular matrix with the size equal to the total number of solids phases. Following Shäfer et al. [29], Silbert et al. [28], Garg et al. [20] and others, the tangential spring and dashpot coefficients are given as a constant fraction of the normal coefficients: $k_t = C_k k_n$ and $\eta_{t,pq} = C_\eta \eta_{n,pq}$. Note that C_η is a scalar, not a tensor. If not specified by the user, the "default" values in MFIX-Exa are $C_k = 2/7$ and $C_\eta = 1/2$, originally owing to Shäfer et al. [29].

Finally, we note another rearrangement of Eqs. (17) and (18),

$$k_n = \hat{m}_{pq}\frac{\pi^2 + \ln^2 e_{pq}}{\left(\delta t_{pq}^{(c)}\right)^2}, \tag{20}$$

giving the spring constant as a function of collision duration. In granular flows it is common, especially when using a Hertzian collision model, for the spring constant to be related to material physical properties such as the Youngs modulus. In CFD-DEM it is much more common to a set the spring constant based on a desired collision duration, which is often set to be "small" compared to the fluid time scales. In this way, particles can be made much softer than in reality, significantly speeding computations with minimal impact on bulk, system hydrodynamics. In this work, the determination of a suitable collision duration (equivalently k_n) will be subject to guess-and-check.

2.4 Particle-Wall interactions

The contact force and torque, $\boldsymbol{f}_{wi}$ and $\boldsymbol{\tau}_{wi}$, from collisions with the walls are computed separately from particle-particle collisions. The collision model is the same as presented in Sec. 2.2 with the obvious adjustments, e.g., $\hat{r}_{ij} = r_j$, $\hat{m}_{pq} = m_p$, etc. The additional terms that must be specified are the particle-wall friction and restitution coefficients, μ_{pw} and e_{pw}, for each p particle phase and a particle-wall spring constant, $k_n^{(w)}$, common to all particles phases. Additionally, there are also particle-wall specific scaling coefficients for the tangential spring and dashpot coefficients. However, with limited evidence to the contrary, these are almost always the same as particle-particle collisions, $C_k^{(w)} = C_k$ and $C_\eta^{(w)} = C_\eta$, which is used throughout this work.

Numerically, a level set function is constructed for embedded boundaries, whether from simple AMReX implicits (e.g., cylinder, box) or complex constructive solid geometry files. The minimum of the level sets signed distance function of is taken as the distance to the contact plane, ℓ_{ci}, for each particle i, which is in contact with a wall if $\ell_{ci} \leq r_i$. Additionally, the collision normal, $\boldsymbol{n}$, is simply the wall normal which is taken as the gradient of the level set function at a value of zero. Because only the minimum level set value is used, e.g., only one ℓ_{ci}, each particle can only have one wall contact at a given time, i.e., no corner contacts with two or three planes of a box at once.

2.5 Numerics

The governing equations of Eq. (1) - (3) are discretized with a simple backward Euler time integration scheme,

$$\frac{I_i^{n+1}\boldsymbol{\omega}_i^{n+1} - I_i^n\boldsymbol{\omega}_i^n}{\Delta t} = \sum \boldsymbol{\tau}_i^n \,, \tag{21}$$

$$\frac{m_i^{n+1}\boldsymbol{u}_i^{n+1} - m_i^{n+1}\boldsymbol{u}_i^{n+1}}{\Delta t} = m_i^n\boldsymbol{g} + \sum \boldsymbol{f}_i^n \,, \tag{22}$$

$$\frac{\boldsymbol{x}_i^{n+1} - \boldsymbol{x}_i^n}{\Delta t} = \boldsymbol{u}_i^{n+1} \,, \tag{23}$$

where $n+1$ and n are the new and old time levels and the summations indicate all forces and torques on particle i. The time step, $\Delta t = t^{n+1} - t^n$, is given as a fraction of the minimum collision time,

$$\Delta t = \frac{1}{C_\Delta} \min\left[\min \delta t_{pq}^{(c)}, \min \delta t_{pw}^{(c)}\right] . \tag{24}$$

This rudimentary numerical scheme is often sufficient in CFD-DEM simulations where the particles are sub-cycled with a particle (DEM) time step which is often orders of magnitude smaller than the fluid (CFD) time step. Further, error introduced by advancing the particles with a frozen fluid field is often thought to dwarf round-off error from the first-order scheme and the largest source of numerical error is assumed to be statistical error, i.e., finite statistical certainty in quantities of interest due to randomness–whether true randomness due to an unknown initial particle configuration or the pseudo-randomness found applying Ergodic theory to a single fluctuating steady state. This typical multiphase reasoning may not be as applicable to purely granular flows.

Although only cold flow studies are considered herein, we note that the particle mass and species fractions are updated first, then the velocities and position, as shown, followed by the particle enthalpy [30]. In MFIX-Exa, each i-j collision is calculated just once, for particle i or j, depending on which appears first in memory. While the normal and tangential forces are symmetric, i.e., $f_{ji} = -f_{ij}$, the contact torque between two particles is not necessarily symmetric due to possible differences in the distance to the collision plane, $\ell_{cj}\boldsymbol{n} \neq -\ell_{ci}\boldsymbol{n}$, and $\boldsymbol{\tau}_{ji}^{(c)}$ is computed for particle j using Eq. (14). Finally, we note that particle walls, either fixed or moving, are not a feature of either `develop` or `!1245` and have been "hacked" into the codes by forcing $\boldsymbol{u}_i^{n+1} = \boldsymbol{u}_i^n$ and $\boldsymbol{\omega}_i^{n+1} = \boldsymbol{\omega}_i^n$ for specific particle phases.

Chapter 3: Oblique Collision

3.1 Setup

For the first test of the full collision model, i.e., including the tangential history term in `!1245`, we consider a single particle-wall collision. This test has been considered in a number of experimental works, most notably the experiments of Kharaz, Gorham, and Salman [1]. In the experiment, a single aluminium oxide particle is dropped onto a thick soda-lime glass anvil with varying degrees of incident inclination angle, θ_i, so that the collision can be adjusted from normal to glancing. The particle properties are provided in Table 1. The distance between the release point and the anvil is fixed so that the impact velocity is constant, which is estimated as $u_i = 3.9$ m/s. A camera is used record the rebounding velocity, u_r and v_r, and angular velocity, ω_r. The normal and tangential restitution coefficients are measured from $e_n = v_r/v_i$ and $e_t = u_r/\left(v_i \tan\theta_i\right)$. The rebound angle is measured from $\theta_r = \tan^{-1} v_r/u_r$. So far, all of these properties are referring to the

center of mass of the particle. The final reported quantity is the rebound angle of the contact patch, i.e., the point on the particle surface that impacts the anvil, which is measured as $\theta_r^* = \tan^{-1}\left(u_r - r_p\omega_r\right)/u_r$.

In the simulations, the experiment is transformed by rotating the frame of reference by $-\theta_i$ so that the wall is always horizontal, $\boldsymbol{n} = (0\,, 1\,, 0)$. 85 particles are placed above the bottom wall separated by $\delta z = 10$ mm. The particles sweep a collision angle from $\theta_i = 1^\circ$ to 85°, each incremented by 1°. The initial particle velocity is given by

$$\begin{aligned} u_i &= |\boldsymbol{u}_i| \sin\theta_i \\ u_i &= |\boldsymbol{u}_i| \cos\theta_i \\ w_i &= 0 \end{aligned}$$

where $|\boldsymbol{u}_i| = 3.9$ m/s, i.e., u_i measured in the experiment. The incident angle of each particle is simply $\theta_i = \mathrm{i}\pi/180$ where i is the particle index, 1 to 85. Each particle is placed at a position so that it takes $\delta t = 2$ ms for the particle to collide with the x-centerline of the domain,

$$\begin{aligned} x_0 &= L_x/2 - \delta t\,|\boldsymbol{u}_i| \sin\theta_i \\ y_0 &= d_p/2 + \delta t\,|\boldsymbol{u}_i| \cos\theta_i \\ z_0 &= \mathrm{i}\delta z \end{aligned}$$

The simulation is run for $2\delta t = 4$ ms and the rebound particle velocities, u_r, v_r and ω_r are used to determine the coefficients of restitution, the rebound angle and the rebound angular momentum. We note that the angular momentum is unsigned and actually directed in the $-z$-direction, i.e., $\boldsymbol{\omega}_r = (0\,, 0\,, -\omega_r)$.

Table 1: Summary of simulation parameters for single particle oblique collisions.

domain		
Width	L_x	0.8 m
Height	L_y	1.0 m
Depth	L_z	1.0 m
particle properties		
diameter	d_p	5.0 mm
density	ρ_p	4000 kg/m^3
collision properties		
restitution coefficient	e_{pw}	0.98
friction coefficient	μ_{pw}	0.092
normal spring stiffness	k_n	1.72e+7 N/m
tangential spring coefficient	C_k	0.86
tangential dashpot coefficient	C_η	0.5
time step coefficient	C_Δ	50

3.2 Results

The particle properties, see Table 1, were taken from Di Renzo and Di Maio [2] who also compared numerical solutions to the data of Kharaz, Gorham, and Salman [1]. Di Renzo and Di Maio [2] used a Hertzian normal force model coupled with the micro-slip theory of Mindlin and Deresiewicz. They also considered a simpler "no-slip" model which is quasi-linear in the tangential overlap, although still depends on the square root of the normal overlap. The data for this model has also been digitized with the experimental data and compared with MFIX-Exa predictions in Fig. 2. When the full linear tangential force is considered as implemented in `!1245`, the results compare very favorably to both the experimental data and the model of Di Renzo and Di Maio [2]. The tangential restitution coefficient, e_t, shows the sharp decay with increasing inclination angle to a minimum at approximately $\theta_i = 20^\circ$, and the increases towards one as $\theta_i \to 90^\circ$. The rebound angle of the contact patch, θ_r^*, bottom set of curves and square data points in the middle figure of Fig. 2, initially increases, then becomes negative due to the rotation of the rebounding particle, then increases to meet θ_r

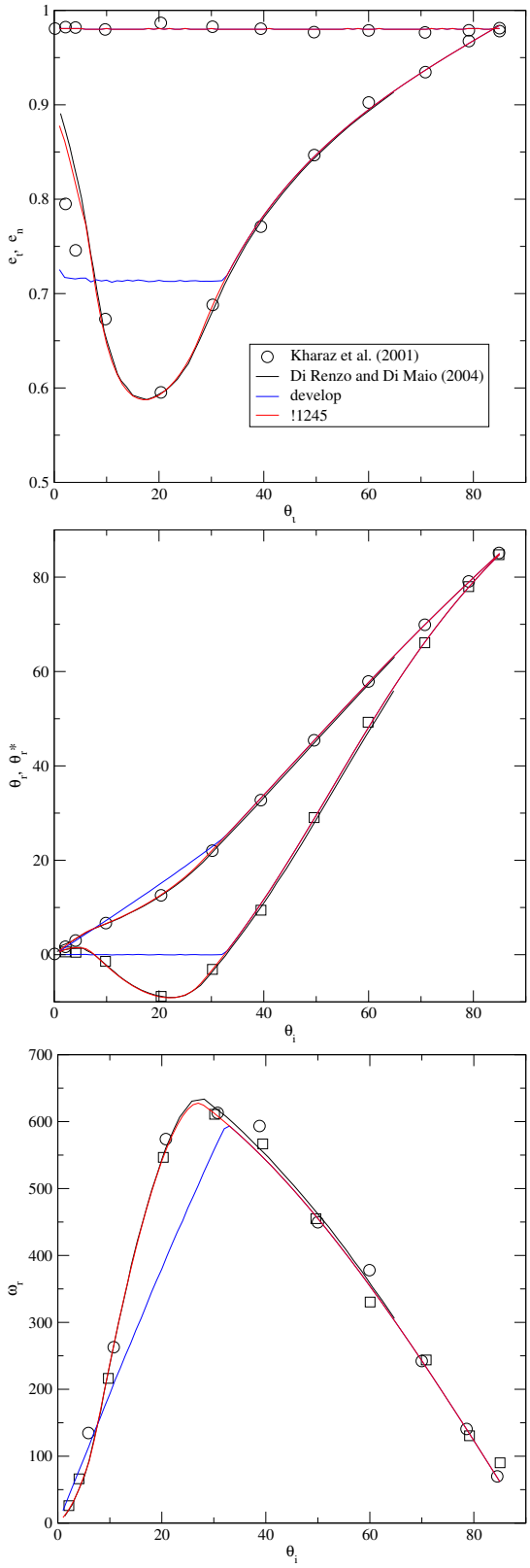

Figure 2: Comparison of MFIX-Exa results with the experimental data of Kharaz et al. [1] and the no-slip Hertzian-Mindlin-Deresiewicz model of Di Renzo and Di Maio [2] for single particle oblique collisions with a solid wall.

with increasing angle. The rotation, ω_r, increases sharply at first, reaches a maximum around $\theta_i = 23°$. (Note that the experimental data for ω_r show measured values as circles and calculated values using the measured tangential restitution coefficient as squares.) The truncated model in MFIX-Exa `develop` shows some clear discrepancies. Perhaps most obviously, the restitution coefficient is initially constant (with some noise) with a value of $e_t = 0.71$ until an angle of approximately $\theta_i = 33°$ before matching the `!1245` result. This result compares well to a similar finding by Capecelatro et al. [12]. An analogous result is seen for the rebound angle of the contact patch, θ_r^*. The rebound angle (of the center of mass) and the angular velocity show the correct trends but with a linear dependence rather than the more complex behavior reproduced by the full model. Clearly, the near-normal regime are the types of collisions for which the static force is important, with glancing collisions being dominated by dynamic (Coulomb) friction force so that the simplified model is sufficient. We end this section by noting that even in the case of the largest discrepancy of the simplified model, the resulting error is relatively minor for single collisions. If the tangential rebound velocity is 20% higher or lower for near-normal collisions, this likely has little impact in the overall dynamics of a large, driven system such as a fluidized bed. However, as will be shown in Sec. 4, the tangential history term can be significant in dense granular systems.

3.3 Parametric study

In this section we explore how these results change by adjusting certain parameters and including rolling friction. To be clear, we are not attempting to improve the agreement observed in Fig. 2. The data, model of Di Renzo and Di Maio [2] and the `develop` results have been dropped. In each subsequent figure, only one parameter is changed at a time from the `!1245` model used to generate the results in Fig. 2.

First, we include rolling friction models, starting with Model A in Fig. 3. The rolling friction coefficient is increased two orders of magnitude from $\mu = 1 \cdot 10^{-4}$. The rebound angles change little in this range; the maximum angular velocity decreases with increasing μ_r, but not substantially. The most noticeable, and seemingly nonphysical, impact is on the tangential restitution coefficient at near normal impacts. For the largest value of μ_r at the smallest incident angle, $\theta_i = 1°$, e_t is actually negative, indicating that the particle has actually rebounded with $u < 0$. For smaller, and more reasonable values of μ_r, the e_t curve only curls down as $\theta_i \to 0$. Unfortunately the experimental data is too sparse to indicate if this behavior is physical or not.

Next we consider rolling friction Model B in Fig. 4 with the rolling friction coefficient increasing two orders of magnitude from $\mu_r = 1 \cdot 10^{-3}$ s/m. This model has a more substantial impact on the solution. While the e_t curve does not bend down through zero, it does decrease with increasing μ_r in the near-normal regime. The angular velocity decreases more significantly, not only at the maximum but throughout the θ_i-range. The decreased ω_r impacts θ_r^* and even a minor effect on θ_r at small $theta_i$ can be observed.

The tangential spring constant is considered in Fig. 5 by varying the coefficient $C_k = k_t/k_n$ from 1 to a little under 0.3. Surprisingly, this has a significant impact on the solution, although restricted to the near-normal regime, specifically for $\theta_i < 30°$. As C_k (and k_t) decreases, the local maximum of e_t near $\theta_i = 0$ is pulled down until a little below $C_k = 0.4$, e_t is a constant from $0° < \theta_i < 20°$. This result us unchanged for a range of lower values of C_k, including $C_k = 2/7$ as shown in Fig. 5. Although e_t decreases with decreasing C_k, ω_r increases until it becomes linear in θ_i up to the maximum. These results are surprising because the lowest value, $C_k = 2/7$ is the recommended value in MFIX-Exa and also the default value in MFiX. This value comes from Shäfer et al. [29], also studying oblique particle collisions. In their work, Shäfer et al. [29] observed that "it does not seem to make much of a difference which value of $[C_k]$ is chosen." However, it should be noted that they did not consider e_t in their work and the value of the friction coefficient may have been higher. Regardless, the findings in Fig. 5 are in stark contrast to the findings of Shäfer et al. [29] and a larger value of C_k may need to be considered going forward.

On the other hand, the tangential dashpot is varied in Fig. 6 by adjusting C_η from 1 to 0.2. The results are virtually indistinguishable. For this parameter we can borrow from Shäfer et al. [29] and say that it does not seem to make much of a difference which value of C_η is chosen.

So far, we have used a spring constant that was chosen by Di Renzo and Di Maio [2] to reproduce a measured collision duration, $\delta t_{pw}^{(c)}$. While not exactly a material parameter, such as selected for their Hertzian model, this high value approximates the stiffness of a realistic collision. In CFD-DEM it is most typical to select a suitable collision time that is roughly an order of magnitude below the hydrodynamic time scales, and

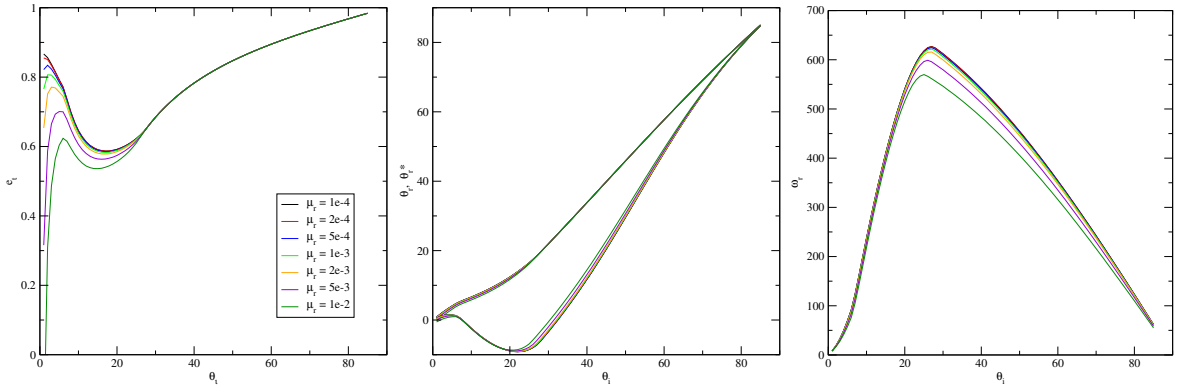

Figure 3: MFIX-Exa `!1245` results for oblique collisions with varying rolling friction coefficient, μ_r, with model A.

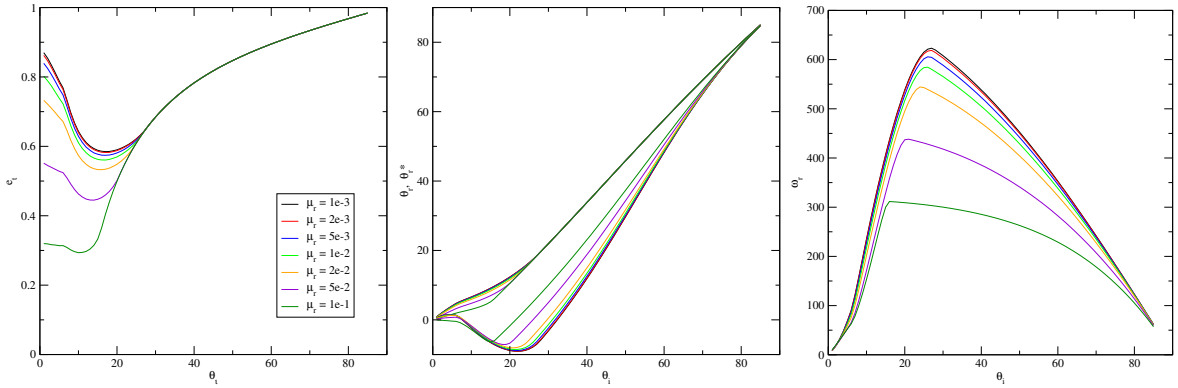

Figure 4: MFIX-Exa `!1245` results for oblique collisions with varying rolling friction coefficient, μ_r, with model B.

set k_n using Eq. (20). For the current value of $k_n = 1.72 \cdot 10^7$, the collision duration is $\delta t_{pw}^{(c)} = 8.67 \cdot 10^{-6}$ s; typical values in CFD-DEM may be 10^{-4} or higher [31, 32, 33]. In Fig. 7, k_n is adjusted to vary $\delta t_{pw}^{(c)}$ two orders of magnitude from 10^{-5}. For the first order of magnitude, i.e., up to $\delta t_{pw}^{(c)} = 10^{-4}$, the results are acceptable with the most noticeable error being a slight decrease in e_t in the near-normal regime. The error becomes more significant as $\delta t_{pw}^{(c)}$ increases above 10^{-4} with the results resembling high rolling friction coefficient values for Model B, compare with Fig. 4. Clearly, k_n is too soft for approximately $\delta t_{pw}^{(c)} > 2 \cdot 10^{-4}$.

Finally, we consider the time step (subcycling) coefficient, $C_\Delta = \delta t_{pw}^{(c)} / \Delta t$. In granular flows, C_Δ is often 50 or as high as 100 [2, 34, 35, 36]; in CFD-DEM–especially for the first author–it is more common to relax this value down to 20. For the reference spring stiffness, C_Δ is varied from 10 to 100. For $C_\Delta > 50$ the results are converged and visually indistinguishable. Even for C_Δ down to 10, the results are very similar. However, as shown in Fig. 8, if we zoom in on the e_t minimum, it is clear that the lowest values of C_Δ have introduced some numerical noise. This result indicates that at least $C_\Delta \geq 30$ is probably required to minimize numerical error in granular simulations.

Chapter 4: Static Piles

In this section we investigate static piles, i.e., heaps of particles at rest. As it turns out, how the piles are formed matters. Two configurations are considered, each with experimental data. In both cases, the experiments begin with a static bed of particles in a container resting on a support which is removed (in places) causing granular motion. In the first case, there is a single opening and the pile that forms in the lower container is of interest. This is referred to as a constrained pile. In the second case, both ends of the

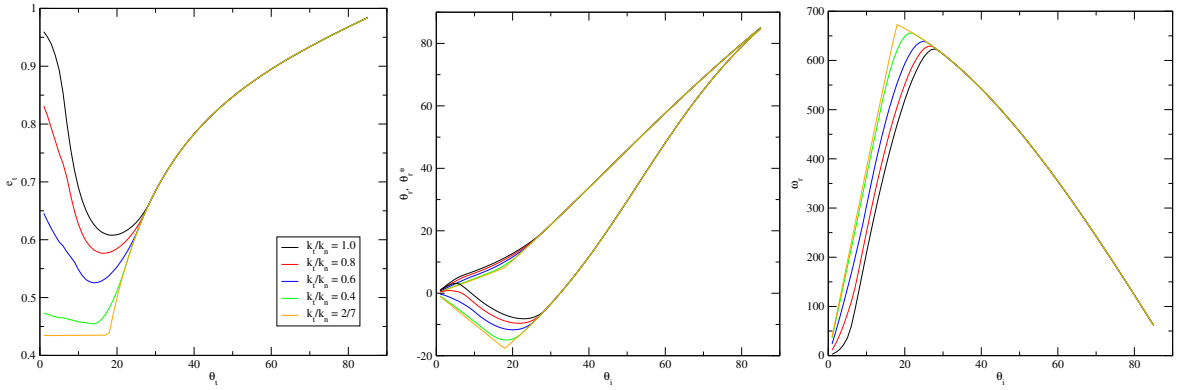

Figure 5: MFIX-Exa `!1245` results for oblique collisions with varying tangential spring stiffness coefficient, C_k.

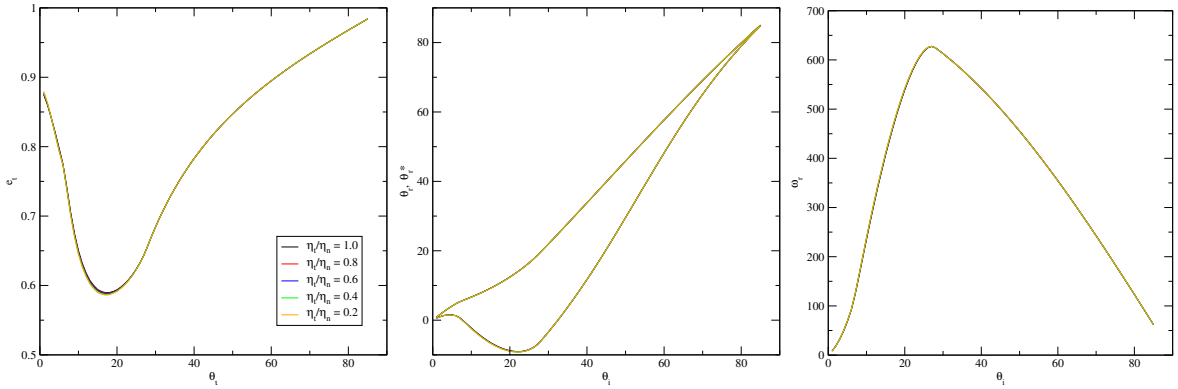

Figure 6: MFIX-Exa `!1245` results for oblique collisions with varying tangential dashpot coefficient, C_η.

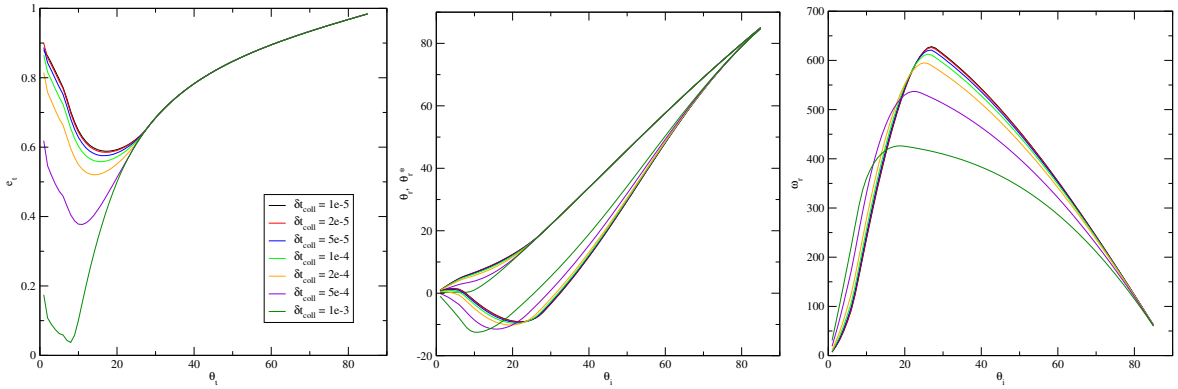

Figure 7: MFIX-Exa `!1245` results for oblique collisions with varying collision time, $\delta t_{pw}^{(c)}$ coll.

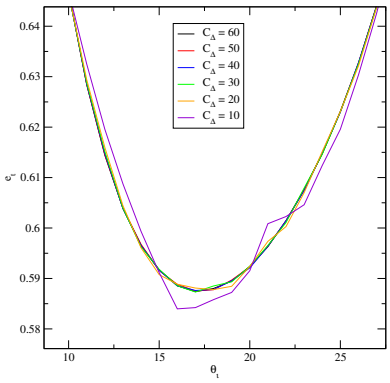

Figure 8: MFIX-Exa `!1245` results for oblique collisions with varying time step coefficient, $C_{\Delta t}$.

support are removed. A V-shaped pile is formed below, but, here the pile of interest is what remains above the support that remains in place. This is referred to as a free pile.

4.1 Constrained pile

The experiment Li et al. [3] consists of a pair of nested boxes. All of the particles are originally contained within the inner box, which is raised, allowing the particles to spill out into the outer box. The outer box has a width and depth of $L_x = 418$ mm and $L_z = 78$ mm. In the original experiment, the outer box had a height of 260 mm. In the model, summarized in Table 2, a slightly shorter box is considered, $L_y = 240$ mm, which is still sufficiently high to contain the final piles. A uniform grid of $24 \times 12 \times 4$ is applied with a mesh size $dx = 20$ mm. The container is modeled with a `box` EB within the full domain. Only the lower plate of the inner box is modeled, which is done so with a rectangular array of 5 mm particles which are given a uniform translation corresponding to the raising of the inner box. The wall particle array has a gap, i.e., the opening which particles spill out of, of size $\delta l_x = 30$ mm and $\delta l_z = 60$ mm, the latter of which corresponds to the physical dimension of the inner box. There are two locations for the gap, either in the center or on the left. For the center gap, δl_x corresponds to the distance between particle edges, i.e., 40 mm between particle centers within the same z-row. For the left-hand gap, δl_x corresponds to the distance between the EB and particle edge.

The actual particles are a tri-disperse mixture of diameter $d_p^{(1)} = 13$ mm, $d_p^{(2)} = 12$ mm and $d_p^{(3)} = 11$ mm numbering $N_p^{(1)} = 750$, $N_p^{(2)} = 1500$, and $N_p^{(3)} = 750$. Other than size, the properties of the glass beads are assumed to be monodisperse with measured density of $\rho_p = 2456$ kg/m^3 and particle-particle and particle-wall kinetic friction coefficients of $\mu_{pp} = 0.15454$ and $\mu_{pw} = 0.1333$, respectively. A coefficient of restitution of $e_{pp} = e_{pw} = 0.98$ is assumed for all types of particle and wall collisions. The minimum collision duration occurs between two of the smallest particles, $\delta t = \delta t_{1-1}^{(c)}$. The spring constant is set to $k_n = 211170$ (N/m), and $k_n^{(w)} = 2k_n$, giving $\delta t = 0.2$ ms. The subcycling coefficient is $C_\Delta = 32$.

The "wall particles," i.e., the artificial particles used to model the lower plate, are given the same collision properties as the real particles. The diameter is $d_p^{(w)} = 5$ mm. Because the wall particles are much smaller than the real particles, they are made very dense, $\rho_p^{(w)} = 5 \cdot 10^5$ kg/m^3, so that they do not affect the timestep.

The tri-dispersed particles are generated in a random array and allowed to settle under gravity for 1 s so that most of the motion has slowed and the particles form a dense bed. The end state of this initialization is used to generate a new initial condition for the primary simulations. The particles are raised by 5 mm and the wall particles are placed underneath, with either a center or left opening. This causes an initial perturbation as the particle bed adjusts from laying on a flat plate to hovering slightly above a (semi-)spherical array. In order to capture the statistical uncertainty in the DEM simulation method, ten different randomized initial conditions are considered. These ten configurations are used for all subsequent simulations and the results are reported as a mean of the outcome with a 95% confidence interval (CI) given by a t-distribution.

A visualization of a typical simulation is shown in Fig. 9 for center opening (left column) and right opening

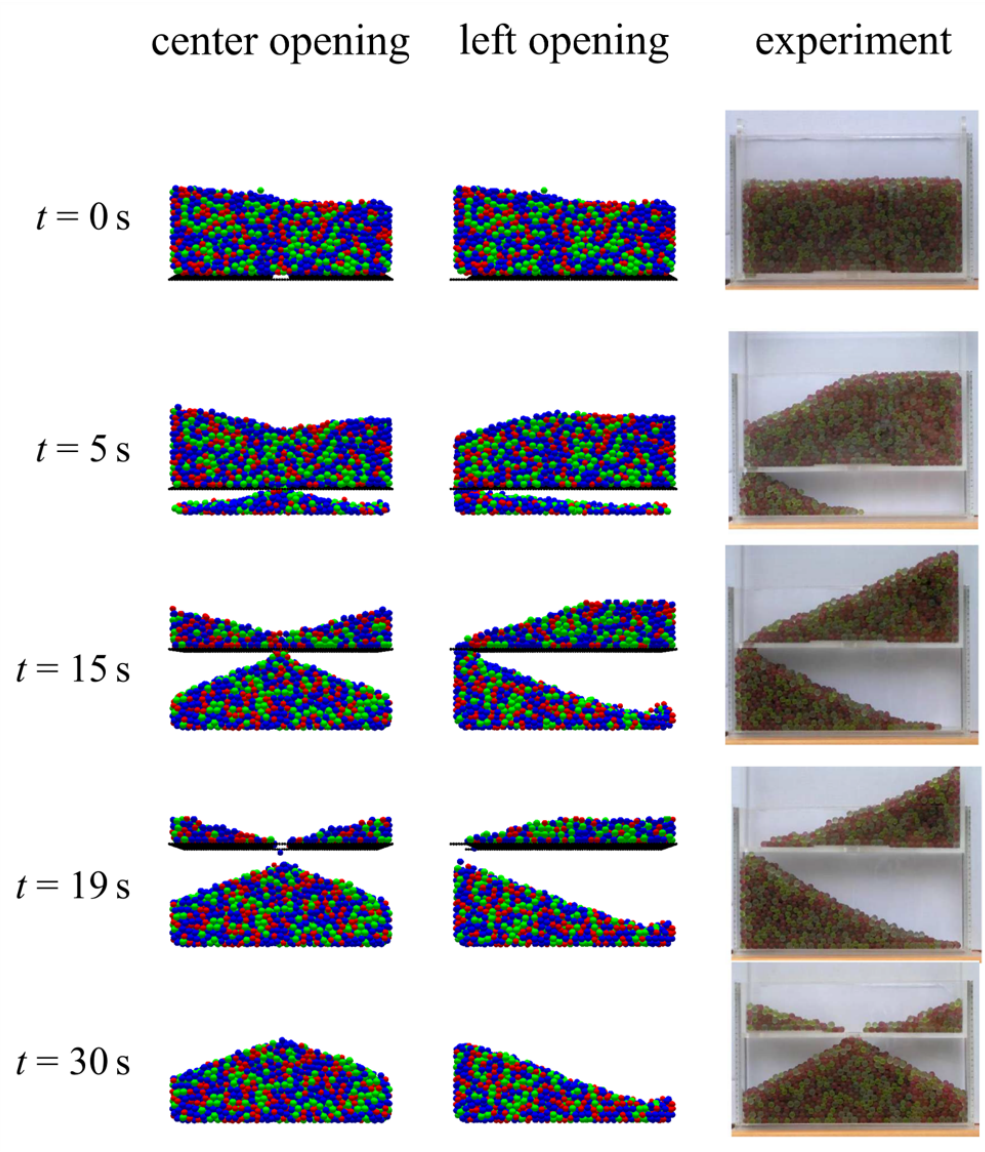

Figure 9: Visualization of a tangential history (`!1245`) simulation using the model settings provided in Table 2 without rolling friction. At right, the experiment [3] for the left opening is shown at times 0, 5 and 15 s, corresponding to the simulation times. The last two rows of the right column show the final conditions (time unknown) of left and center opening experiment, respectively.

Table 2: Summary of simulation parameters for the constrained pile of Li et al. [3].

domain		
Width	L_x	418 mm
Height	L_y	240 mm
Depth	L_z	78 mm
particle properties		
diameter	$d_p^{(1)}$	11 mm
diameter	$d_p^{(2)}$	12 mm
diameter	$d_p^{(3)}$	13 mm
density	ρ_p	2456 kg/m^3
collision properties		
p-p restitution coefficient	e_{pp}	0.98
p-w restitution coefficient	e_{pw}	0.98
p-p friction coefficient	μ_{pp}	0.1333
p-w friction coefficient	μ_{pw}	0.1545
normal spring stiffness	k_n	211170 N/m
tangential spring coefficient	C_k	0.9
tangential dashpot coefficient	C_η	0.9
time step coefficient	C_Δ	32

(middle column). The left-opening experiment is shown in the right column for the first three times, and the final times of the left and center opening experiments are shown in the final panels. This simulation utilizes the tangential history term implemented in `!1245` but no rolling friction. It can be seen, even qualitatively in Fig. 9, that the final piles are not as steep as the corresponding experiments. Note that the simulations shown in Fig. 9 had a final angle of repose closest to the mean of the ten replicates, i.e., the values reported in Table 3. The comparison of the left opening at $t = 5$ s is also noteworthy. The experiment shows a triangular pile with some "spillage" near the bottom that extends to roughly the x-centerline of the box; the simulation shows that the discharged particles have run all the way to the opposite wall. The wall particles move up with a velocity of 10 mm/s. This is faster than used by Li et al. [3], however the comparisons between simulation and experiment at times $t = 5$ and 15 s are quite agreeable–if anything, the experiment appears to be slightly faster. By $t = 24$ s, the bottom plate vanishes out of the pressure outlet at $y = L_y$ along with any real particles that had remained on top of it. The bed is allowed to come to rest awhile longer, ending at $t = 30$ s, at which point the angle of repose is measured.

The angle of repose is measured by first binning the particles into 5 mm bins spanning the width of the bed. The 1-D elevation, $h(x)$, is found by taking the center of the highest particle contained in each bin. Because the width of the bed is not an integer product of the bin width, the excess space is given to the center bins for the center opening simulations and to the right most bin for the left opening experiment. The angle of repose, θ_R, is determined from a linear fit to $h(x)$. The individual results for the cases visualized in Fig 9 are shown in Fig. 10. For center opening simulations, two θ_R results are taken, for the left- and right-side slopes. Note that $\theta_R^{(right)}$ and $\theta_R^{(left)}$ should not be statistically different because the simulation is symmetric. For the center opening, the two bins nearest the walls and the four central bins *of each* left and right $h(x)$ are ignored to eliminate wall effects and some rounding off of the top of the pile. For the left opening, two bins on the left are ignored and four on the right. This was necessary because the particles tended to run up the right-side wall early in the simulation, see Fig. 9 at $t = 15$ s.

Simulations were run with (`!1245`) and without (`develop`) the tangential history term. For both configurations, the tangential history term increases the angle of repose by approximately 3°. However, this is still significantly lower than the $\theta_R = 26°$ measured in the experiment. Increasing the friction coefficient–here we have increased both μ_{pp} and μ_{pw} together–improves the agreement. Without tangential history, this increases θ_R to approximately the that of the tangential history model with the measured friction coefficient values. Increasing the friction coefficient, μ, with tangential history gets the angle repose for the center opening almost inline with experimental result. However, the left opening is still low. Note that the discrepancy

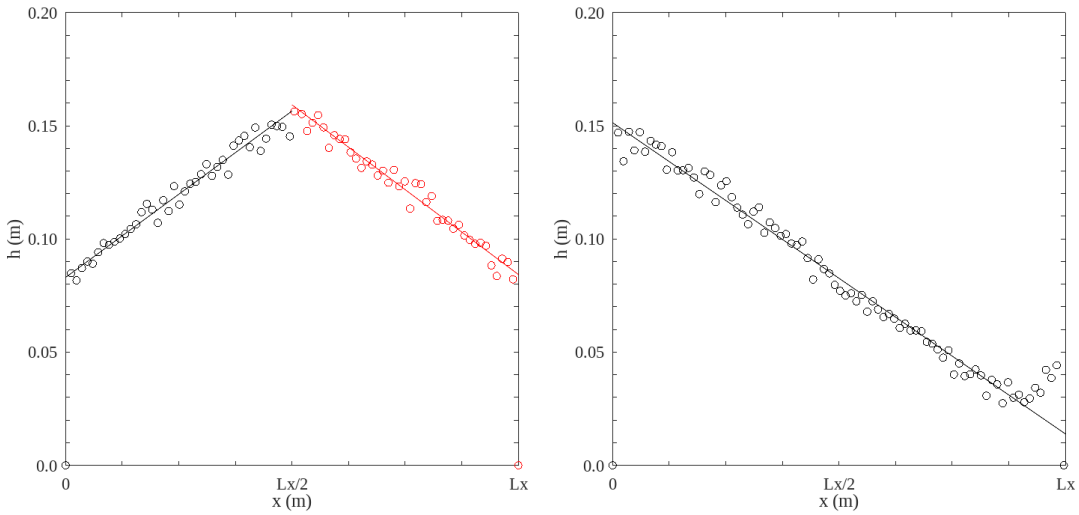

Figure 10: Angle of repose measurements for the cases shown previously in Fig. 9. Circles show the discretized particle height function, $h(x)$, and lines show the linear fits.

Table 3: Summary of angle of repose simulation results ($\theta_R^{(left)}$ and $\theta_R^{(right)}$ correspond to the center opening; θ_R corresponds to the left opening).

model	$\theta_R^{(left)}$	$\theta_R^{(right)}$	θ_R
`develop`	16.38 ± 0.91	17.06 ± 0.78	15.46 ± 0.37
`develop` w/ $\mu = 0.3$	18.75 ± 0.57	18.70 ± 0.61	18.57 ± 0.31
`develop` w/ $\mu = 0.6$	19.54 ± 0.47	19.44 ± 0.73	19.34 ± 0.25
`!1245`	19.48 ± 0.64	19.31 ± 0.96	18.06 ± 0.44
`!1245` w/ $\mu = 0.3$	24.50 ± 0.70	23.96 ± 0.93	21.35 ± 0.30
`!1245` w/ $\mu = 0.6$	26.07 ± 0.61	26.24 ± 0.74	22.39 ± 0.28
`!1245` w/ model A $\mu_r = 10^{-4}$	20.20 ± 0.77	20.21 ± 0.69	18.32 ± 0.43
`!1245` w/ model A $\mu_r = 10^{-3}$	19.57 ± 0.88	20.33 ± 0.58	18.63 ± 0.34
`!1245` w/ model A $\mu_r = 10^{-2}$	20.77 ± 0.63	20.69 ± 0.62	18.92 ± 0.26
`!1245` w/ model B $\mu_r = 10^{-3}$	19.57 ± 0.88	20.33 ± 0.58	18.63 ± 0.34
`!1245` w/ model B $\mu_r = 10^{-2}$	19.73 ± 0.82	20.18 ± 0.90	18.32 ± 0.43
`!1245` w/ model B $\mu_r = 10^{-1}$	20.02 ± 1.04	20.00 ± 1.17	18.47 ± 0.26

between the center opening θ_R's and the left opening θ_R is not observed in the experiment which reported $\theta_R = 26.3°$ for center opening and $\theta_R = 26.4°$ for left opening [3]. Interestingly, when rolling friction is included–with μ_r of both models varied over three orders of magnitude–there is no impact on the angle of repose for either configuration. This is in stark contrast to the findings of Zhou et al. [4] who reported that "a larger rolling friction coefficient leads to more spheres in the stagnant zone and a larger angle of repose." Finally, we note that for all cases reported in Table 3, $\theta_R^{(left)}$ and $\theta_R^{(right)}$ are *not* statistically significantly different, in accordance with our assumption of a symmetric system.

4.2 Free pile

In this section we attempt to address one of the glaring inconsistencies of the previous section: the lack of an influence of rolling friction on the angle of repose. Here, we consider a slightly different static pile formation method. Again, particles are filled into a container and discharged into a reservoir. However, here, we are now concerned with the particles that remain in the initial, elevated region.

The model and particle properties, summarized in Table 4, correspond to the experiment of Zhou et al. [4].

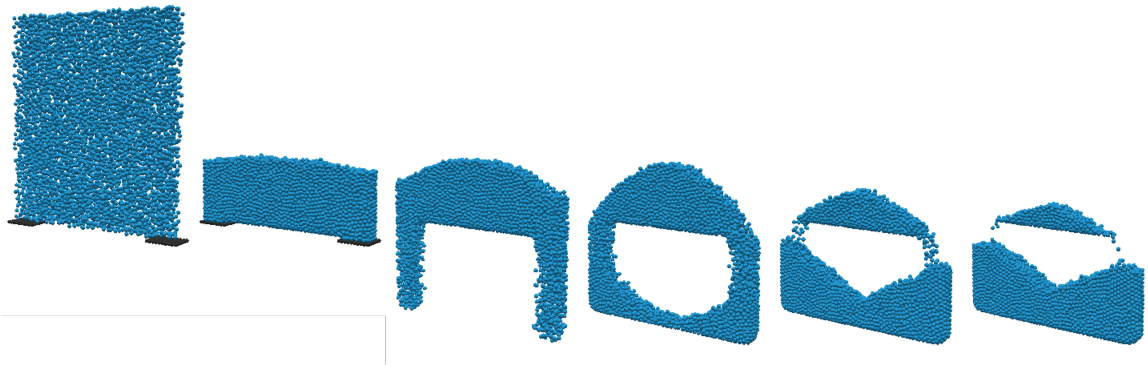

Figure 11: Visualization of the simulation of the experiment of Zhou et al. [4] with time advancing from left to right: $t = -2.0$, 0^-, 0.16, 0.32, 1.0, and 3.0 s. Note that the EB support is not shown.

The container is of width $L_x = 300$ mm and depth $L_z = 40$ mm. The total height of the domain is taken to be $L_y = 600$ mm. A uniform grid of $24 \times 48 \times 4$ is applied with a of mesh size $dx = 12.5$ mm. In the experiment, a wooden block of unspecified thickness is fixed such that the upper plane is located at an elevation of $y = 150$ mm. The fixed support spans the depth of the container but is only 200 mm in width. Adjustable supports initially fill in the open 50 mm gaps at either end. After particles are filled in and allowed to settle, the adjustable supports are abruptly removed or retracted, causing the particles to discharge into the open zone below the support. (Exactly how this is achieved is unknown.) In the model, both the container and fixed support are modeled with a single EB constructed from a `csg` format file. The thickness of the fixed support is 25 mm (two mesh cells). The removable supports are modeled with wall particles, discussed below.

Table 4: Summary of simulation parameters for the free pile of Zhou et al. [4].

domain		
Width	L_x	300 mm
Height	L_y	600 mm
Depth	L_z	40 mm
particle properties		
diameter	d_p	6 mm
density	ρ_p	2500 kg/m^3
collision properties		
p-p restitution coefficient	e_{pp}	0.4
p-w restitution coefficient	e_{pw}	0.7
p-p friction coefficient	μ_{pp}	0.4
p-w friction coefficient	μ_{pw}	0.7
normal spring stiffness	k_n	14800 N/m
tangential spring coefficient	C_k	0.9
tangential dashpot coefficient	C_η	0.9
time step coefficient	C_Δ	32

The experiment considered two sizes of glass beads, $d_p = 10$ and 6 mm. Here we only consider the latter, for which there are 6000 particles of diameter $\rho_p = 2500$ kg/m^3. We note that the collision properties, given in Table 4, are very dissipative compared to what is typically used for glass beads. The spring constant is set to $k_n = 14.8$ (kN/m), and $k_n^{(w)} = 2k_n$, such that $\Delta t = 10^{-5}$ s with a subcycling coefficient of $C_\Delta = 32$. The wall particles are $d_p^{(w)} = 5$ mm with the same collision properties as the real particles. The density is set to $\rho_p^{(w)} = 2\rho_p$ so as not to affect the timestep.

Unlike the setup in the previous section, the wall particles are included in the domain during the

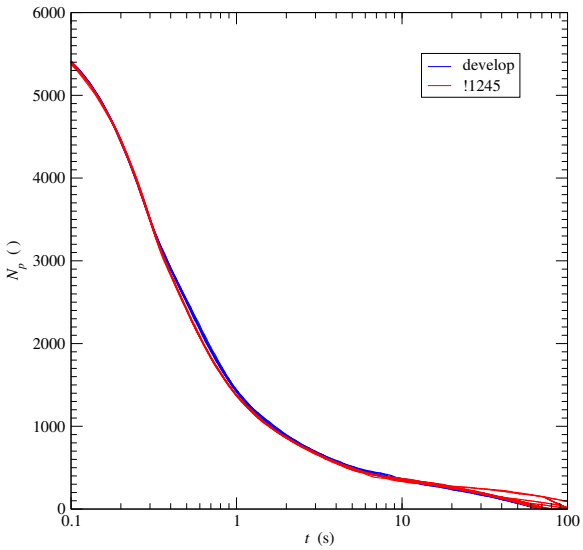

Figure 12: Comparison of the number of particles remaining in the domain without (`develop`) and with tangential history (`!1245`).

initialization so that no collision details are lost, i.e., avoiding the tangential history being re-set by a new initial condition. The particles are randomized above the support and allowed to come to rest for 2 s at which point the wall particles are abruptly deleted. The static particle bed abruptly falls with the particle supports removed and discharges from both sides, leaving a triangular pile sitting on the fixed (EB) support as shown in Fig. 11. Although most of the dynamics happen within the first few seconds, it can take a long time to reach the infinite time limit behavior of upper pile. To speed up the simulations, the bottom of the domain is chopped off by placing a pressure outflow at an elevation of $y = 100$ mm. Therefore, particles that fall off of the support are simply deleted. The simulations are run for 100 s, which is sufficient for *most* of ten replicate ICs to equilibrate. The result is characterized simply by the number of particles, $N_p(t)$, remaining in the domain.

Figure 12 compares N_p with (`!1245`) and without (`develop`) tangential history. The differences are minimal and the final results are the same: $N_p(t \to \infty) \to 0$. In other words, regardless of whether or not tangential history is included in the collision model, all of the particles run off the support. There is no angle of repose because there is no static pile. This behavior changes when rolling friction is included. Figure 13 compares four orders of magnitude variation in μ_r for rolling friction model A (left) and B (right). Now, particles remain on the support, at least with the larger values of μ_r, note $\mu_r = 10^{-5}$ for model A and $\mu_r = 10^{-4}$ and 10^{-4} s/m for model B are essentially indistinguishable from $\mu_r = 0$. However, Fig. 13 is presented in log-log form to highlight one important difference: piles with model A reaches an equilibrium value; piles with model B continue to shrink in size. This is because the rolling torque of model B depends on the relative rotational velocity at the contact plane. Therefore, as the particles stop rotating the rolling torque vanishes, see Eq. (16), meaning that the results of model B should approach the results of no rolling friction, i.e., no pile at all, as $t \to \infty$ in the absence of external forces.

For model A with rolling coefficient values of $\mu_r = 10^{-2}$, 10^{-3}, and 10^{-4}, the average number of remaining particles are 465, 197, and 78. This highest value is in reasonable agreement with the experiment, reported between 786 ± 11 remaining. This is also in good agreement with the simulations of Zhou et al. [4]. Note that Zhou et al. [4] reported good agreement with a rolling coefficient of 2.5×10^{-5} to 5×10^{-5} m which is a dimensional coefficient that contains the particle radius, see Eq. (15). For comparison, for $\mu_r = 10^{-2}$, $d_p \mu_r / 2 = 3 \times 10^{-5}$. The final piles for rolling friction model A are shown in Fig. 14. Although not visualized, it should be noted that, like the bounding domain itself, the support is rounded at either end. This discrepancy with the simulation method of Zhou et al. [4] might explain the smaller particle count.

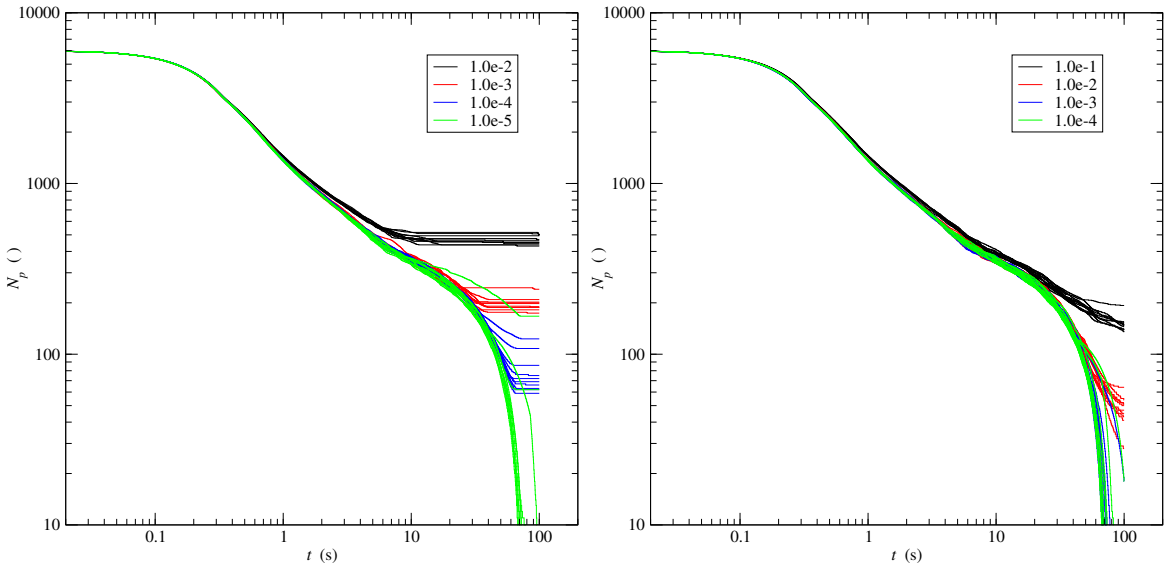

Figure 13: Comparison of the number of particles remaining in the domain with tangential history (`!1245`) and rolling friction model A (left) and model B (right) for different values of the rolling friction coefficient, μ_r.

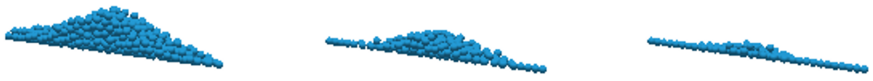

Figure 14: Final ($t = 100$ s) pile formations for the simulations of the experiment of Zhou et al. [4] including rolling friction model A, left to right $\mu_r = 10^{-2}$, 10^{-3}, and 10^{-4}.

Chapter 5: Hopper Discharge

The discharge of a granular material from a hopper is one of the most fundamental industrial problems of interest. In this section, we model and simulate a flat-bottom hopper from the experiments of Beverloo et al. [5] that was used to develop their seminal correlation,

$$\dot{m} = C\rho_b\sqrt{g}\,(D_o - kd_p)^{2.5} \ , \tag{25}$$

where $\dot{m} = dm/dt$ is the mass flow rate, $\rho_b = \phi_0\rho_p$ is the bulk density, D_o is the orifice diameter and C and k are constants. The general form of the widely used Beverloo correlation uses $C = 35$ and $k = 1.4$ which was determined from an average over several granular materials. Here, however, only sand is considered, so the specific best-fit for sand is used, $C = 38.8$ and $k = 2.9$.

Beverloo et al. [5] originally considered a number of hoppers, orifice sizes, orifice shapes and granular materials. For demonstration purposes, we consider only one here. As is now well known, and shown by Beverloo et al. [5], the hopper diameter and the static height of the granular material do not have a significant influence on the discharge mass flow. Therefore, for computational efficiency, we choose the smallest hopper diameter and bed height, $D = 5$ cm and $H_0 = 10$ cm, respectively. For this hopper size, mass flow results are given for orifice diameters of $D_o = 0.25$, 0.50, 0.75, 1.00, 1.25, and 1.50 cm. We select sand as the granular material which has been sieved to a range of 210 to 300 micron. It is assumed that there is a uniform distribution of particle diameters from this minimum to maximum range. The particles are generated uniformly throughout the domain in a hexagonal close packed lattice at a volume fraction of $\phi = 0.32$, roughly half the expected ϕ_0 in twice the volume ($L_y/H_0 = 2$). The particles are given an initial granular temperature, $\sqrt{T_0} = 0.1$ m/s, to prevent the particles from settling into a structured lattice. The particles are seeded into 90 discrete 10 micron bins and the density is constant at the measured value, $\rho_p = 2620$ kg/m^3. The collision properties were assumed and the values used are provided in Table 5. Because all particles are of a single type or phase, the average diameter is used to calculate the collision duration. We set the spring constant to $k_n = 11.237$ N/m (and $k_n^{(w)} = 2k_n$) which gives $\delta t = 10^{-4}$ s with $\bar{d}_p = 255$ micron.

Table 5: Summary of simulation parameters for the hopper simulations.

domain		
Width	L_x	5.0 cm
Height	L_y	20.0 cm
Depth	L_z	5.0 cm
Hopper Diameter	D	5.0 cm
Orifice Diameter	D_o	0.25 - 1.50 cm
Static Bed Height	H_0	10 cm
particle properties		
diameter	d_p	210 - 300 micron
distribution	$\mathcal{F}(N)$	uniform (90 bins)
density	ρ_p	2620 kg/m^3
collision properties		
p-p restitution coefficient	e_{pp}	0.9
p-w restitution coefficient	e_{pw}	0.9
p-p friction coefficient	μ_{pp}	0.25
p-w friction coefficient	μ_{pw}	0.35
normal spring stiffness	k_n	11.237 N/m
tangential spring coefficient	C_k	0.9
tangential dashpot coefficient	C_η	0.9
time step coefficient	C_Δ	32

Although the geometry of the hopper is fixed, the discharge behavior was modeled in several different ways. First, the bottom of a cylinder (the bottom of the hopper) was connected to a smaller cylinder (the orifice) and a pressure outlet was placed just one mesh cell away from this intersection. While this is

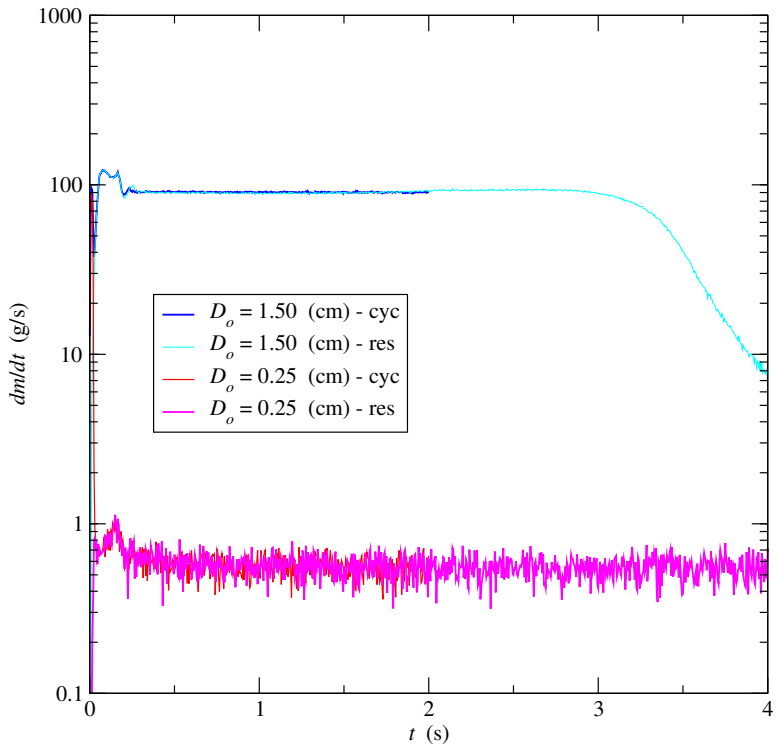

Figure 15: Comparison of hopper discharge mass flow rates between the cyclic and reservoir hoppers for the largest and smallest orifice diameters using `!1245`.

the most computationally efficient setup, we were concerned that the discharge rate might have a strong influence on how particles are deleted as they exit through the pressure outlet. Therefore, a cyclic hopper was considered. In this case, the bottom and top of the domain are a periodic boundary condition. Particles flow out of the exit, reappear at the top of the domain and pour back onto the top of the static bed in this infinitely discharging hopper configuration. While this avoids any direct influence of the BC on the discharge, visualization of this process[1] created a new cause for concern: that the stream of particles impacting the bed may create a significant downward force, not present in the experimental setup, which may affect the results. To test this, a third configuration was considered. The domain was doubled in the vertical dimension and a reservoir, also of $D = 5$ cm, was included.

To begin, the case including the discharge reservoir was only simulated including tangential history (`!1245`) for the largest, $D_o = 1.50$ cm, and smallest, $D_o = 1.50$ cm, orifice diameters. In all cases, a Lagrangian mass flow rate monitor is placed at the bottom of the orifice with a thickness of $\delta y = 10 \min d_p$. The results are compared to the results of their corresponding cyclic hoppers in Fig. 15. In both extremes, it is difficult to distinguish the two configurations from one another for most of the first two seconds of simulation. (Note that $t = 2$ s is the end-of-simulation time for the cyclic hopper configuration because it was determined that a quasi-steady state flow rate could be determined after approximately $t = 0.5$ s for all orifices.) At later times, the results diverge as the reservoir configuration will eventually empty of particles in the hopper, as seen for $D_o = 1.50$ cm slightly after $t = 3$ s in Fig. 15. This result indicates that there is no adverse affect of discharging the hopper back into itself. In fact, the cyclic hopper results appear to be slightly more stable than in the reservoir configuration. Figure 16 shows the time averaged mass flow rates with (`!1245`) and without (`develop`) the tangential history term for all orifice diameters. The simulations tend to over-predict the empirical correlation, but including tangential history significantly improves the comparison. By plotting in a log-log scale, bottom of Fig. 16, we can see that both models show a deviation in $\dot{m}$ earlier, i.e., at smaller D_o, than the correlation predicts.

It appears that most of the improvement with the inclusion of tangential history can be attributed to

[1] http://edx.netl.doe.gov/dataset/baedff18-c799-401b-b02b-7e0795ecd2eb/resource/0a19314d-9b00-4974-8d6b-53152e1f6807

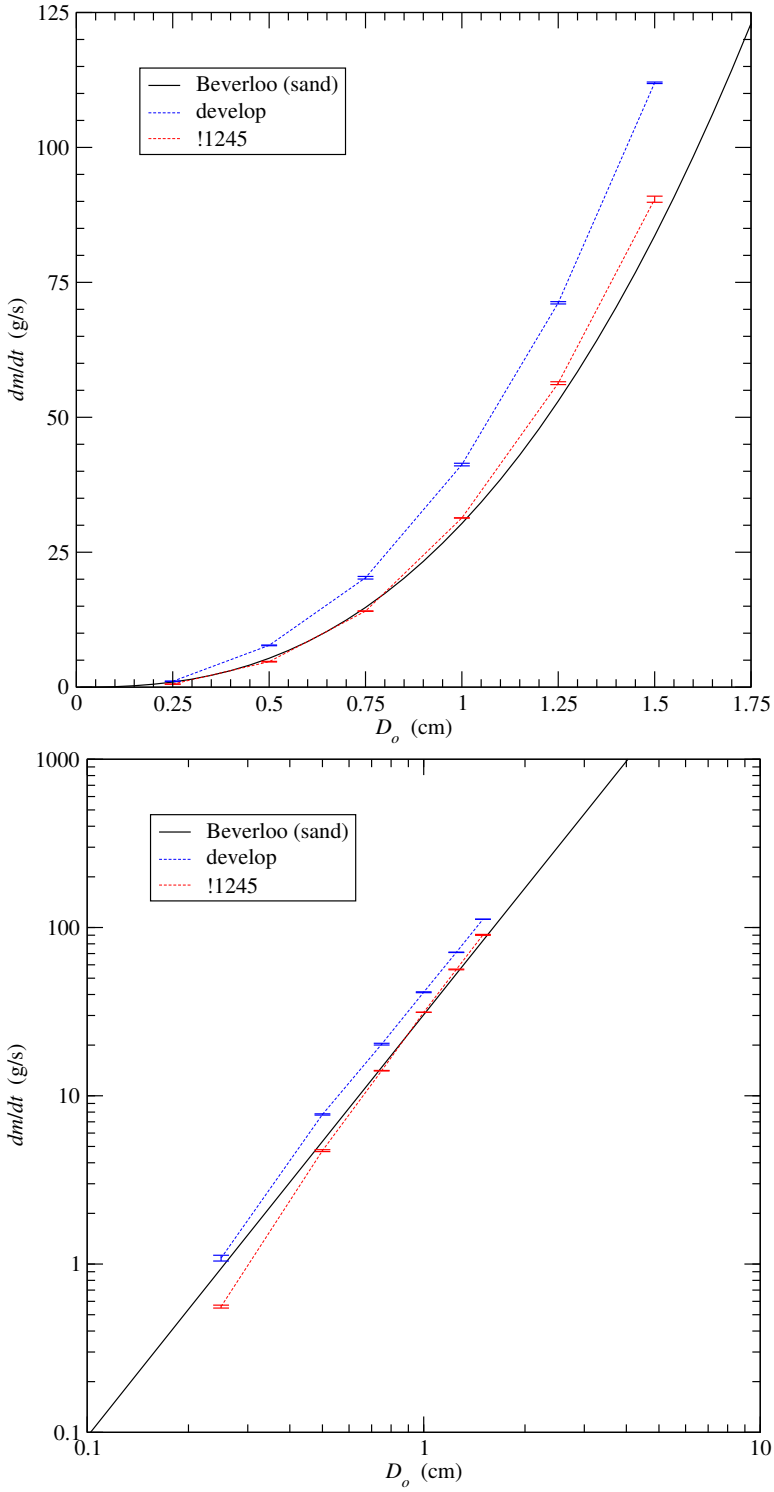

Figure 16: Comparison of the cyclic hopper discharge mass flow rates using the cyclic hopper configuration to the original correlation of Beverloo et al. [5] for sand, i.e., Eq. (25) with $C = 35$ and $k = 1.4$

Table 6: Solids packing fraction in a 5.0 cm tall region near the bottom of the cyclic hopper.

D_o (cm)	ϕ_0 (develop)	ϕ_0 (!1245)
0.25	0.685	0.647
0.50	0.683	0.640
0.75	0.678	0.640
1.00	0.672	0.641
1.25	0.669	0.641
1.50	0.667	0.638

a better estimation of the bulk density, or, equivalently, the solids packing fraction. A volumetric monitor was included to measure the solids volume fraction between elevations of $y = 2$ cm and $y = 7$ cm. It should be pointed out that while this region of the simulation is *relatively* packed, the particles are still in motion as they exit through the orifice and return from above. The time-averaged solids volume fraction for (`develop`) and (`!1245`) simulations are provided in Table 6. With tangential history, the solid volume fraction is relatively steady at 64 % which is consistent with random close packed monodisperse spheres. Without tangential history, the solids volume fraction is slightly higher, increasing from 66.7 to 68.5 % with decreasing orifice diameter. While this may not be excessive for this slightly disperse material, it is significantly higher than reported. For reference, the measured bulk density would give a static packing fraction of $\phi_0 = \rho_b/\rho_p = 57.25$ %.

Chapter 6: Self-Induced Granular Instability

In the final test of the tangential history term, we try to replicate a recently discovered phenomena termed the Self-Induced Granular Rayleigh-Taylor (SIGRT) instability. First reported by D'Ortona and Thomas [34], the SIGRT arises in particles sliding down an inclined plane. The particles are made of a bi-disperse mixture of small, light particles, and larger, heavier particles. The SIGRT pits two instabilities against one another. The Brazil nut effect causes the larger particles to rise to the surface of the flow. Conversely, once a sufficient amount of large (heavy) particles at at the top, this creates a Rayleigh-Taylor instability with a denser layer superimposed over a lighter layer. The RT instability portion, of course, requires that the granular materials be sufficiently fluidized, in this case by gravity (inclination) and surface roughness.

The simulation setup follows that of D'Ortona and Thomas [34]. The small particles have diameter and density, $d_p^{(s)} = 6$ mm, $\rho_p^{(s)} = 1308$ kg/m^3. The large particles are twice as large, $d_p^{(l)} = 2d_p^{(s)}$, and one and a half times as dense, $\rho_p^{(l)} = 1.5\rho_p^{(s)}$. Each are given $\pm 5\%$ variability in diameter, randomly seeded throughout the range, in order to prevent crystallization. The restitution coefficient is $e_{pp} = 0.87$ and the friction coefficient is $\mu_{pp} = 0.7$. There are no wall collision properties because there are no walls in the main simulation. The average diameter of the small particles is used to calculate the collision duration. Assuming the actual average diameter is approximately equal to the mean of the range, $\bar{d}_p^{(s)}$, we set the spring constant to $k_n = 71$ kN/m which gives $\delta t = 10^{-4}$ s. The remaining collision parameters are given with the simulation summary in Table 7.

The domain is set to $L_x = 100\bar{d}_p^{(s)} = 0.6$ m in the flow direction and $L_z = 200\bar{d}_p^{(s)} = 1.2$ m in the spanwise direction. Periodic boundary conditions are used in both x- and z-dimensions. The height or flow thickness is set *a priori* to $H = 36\bar{d}_p^{(s)}$. Assuming a packing fraction of $\phi_0 = 0.64$, the "flow volume" would be filled by approximately 110,000 large particles. For an equal volume ratio of large and small particles, the flow is seeded with $N_p^{(l)} = 55000$ large particles and $N_p^{(s)} = 2^3 N_p^{(s)} = 440000$ small particles.

The simulation is run in three separate stages. The first stage is used to create the ramp surface, i.e., the lower boundary condition. The domain is an `EB` box which is substantially larger than Lx and L_z so as to not interfere with the periodic boundary conditions. The height of the box is set to L_y and shifted down by 4 mm, i.e., the domain extends from $y = -0.004$ to 2.396 m. The ramp is made of small particles without dispersity (i.e., all particles have 6 mm diameter). 40000 particles are seeded in a lower region, $0 < y < 0.1$ m, which is estimated to be approximately twice as many required. The particles are allowed to settle under

Table 7: Summary of simulation parameters for the SIGRT simulation.

domain		
width	L_x	0.6 m
height	L_y	2.4 cm
depth	L_z	1.2 m
flow height	H	0.216 cm
inclination angle	θ	23°
small particle properties		
diameter	$d_p^{(s)}$	5.7 - 6.3 mm
distribution	$\mathcal{F}(N)$	uniform random
density	$\rho_p^{(s)}$	1308 kg/m^3
large particle properties		
diameter	$d_p^{(l)}$	11.4 - 12.6 mm
distribution	$\mathcal{F}(N)$	uniform random
density	$\rho_p^{(l)}$	1962 kg/m^3
collision properties		
p-p restitution coefficient	e_{pp}	0.87
p-p friction coefficient	μ_{pp}	0.7
normal spring stiffness	k_n	71×10^3 N/m
tangential spring coefficient	C_k	0.9
tangential dashpot coefficient	C_η	0.9
time step coefficient	C_Δ	32

gravity for $t = 2$ s. After this initial settling period, all particles with elevations below zero are frozen in place. There are 17958 particles in the ramp for an area fraction $\phi_0^{(2-\mathrm{D})} \approx 0.7$. A head on ($x$-normal) and overhead ($y$ normal) view of the ramp is shown in Fig. 17, indicating that a vast majority of the particles are resting on the EB, i.e., $y_p = -1.0$ mm , and a few particles resting on that layer. All remaining particles are removed.

In the second stage, the large and small particles are seeded in the domain and allowed to settle under gravity for $t = 2$ s on top of the fixed-particle ramp. The particles are seeded randomly and uniformly. Note that in both of the preliminary settling stages, gravity is aligned in the y-dimension, $g_y = -|\boldsymbol{g}| = -9.81$ m/s^2 and $g_x = g_z = 0$. Finally, in the third stage, the ramp is "inclined" by adjusting gravity to $g_x = |\boldsymbol{g}| \sin\theta$, $g_y = -|\boldsymbol{g}| \cos\theta$. The development of the instability is monitored with a simple scalar segregation (mixing) index,

$$I_s = \frac{\bar{y}_p^{(l)} - \bar{y}_p^{(s)}}{H/2} \ . \tag{26}$$

Values of $I_s = -1$, 0 and 1 indicate perfectly segregated with small particles on top, well mixed, and perfectly segregated with large particles on top. For convenience, a simple number average, rather than a volume average, is used to compute the mean particle elevations, effectively neglecting the slight size distributions.

In the first test, nothing happened. Any motion persisting after the settling period decayed to zero and froze into a completely static array. This indicates that perhaps the particle ramp is too rough. In order to "kick start" the third stage, the particles were given a streamwise velocity of $u_p(t = 0) = 0.5$ m/s. (For reference, this is about one third of the long-time, pseudo-steady state, domain averaged streamwise velocity.) This kick did not seem to be too violent and allowed the flow to start developing naturally. The segregation index in Fig. 18 follows the same general trend as that originally observed by D'Ortona and Thomas [34]. We do note, however, that the peak magnitude of I_s is lower here, possibly due to the larger height considered, $H = 36\bar{d}_p^{(s)}$ *versus* $H = 20\bar{d}_p^{(s)}$.

In order to visualize the dynamics of the process, all particles are averaged onto a two-dimensional $z - y$ map and binned into a 100×50 grid of edge size 12 mm (i.e., $d_p^{(s)}$). On this grid the volume averaged fraction of small (and large) particles is computed as well as the volume-weighted velocities of each "phase." We originally tried to examine large- and small-particle velocity profiles separately, but, ultimately, it was simpler

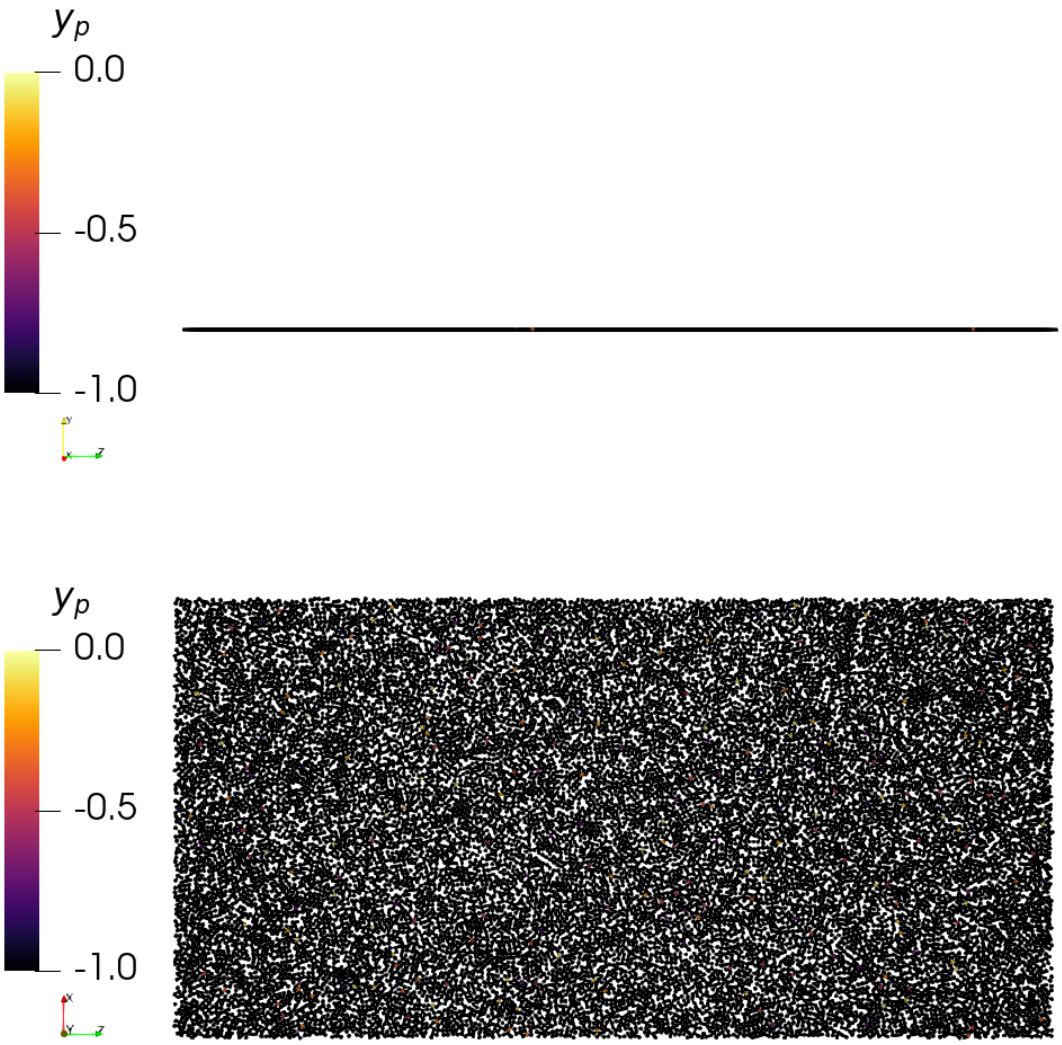

Figure 17: Views of the particles frozen in place to create the ramp; colored by particle center elevation, y_p, in mm.

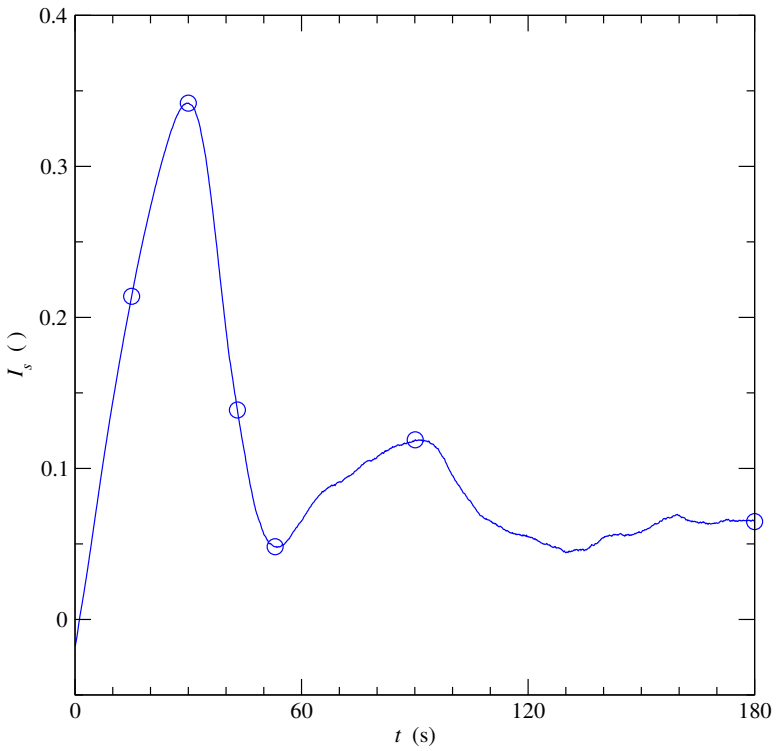

Figure 18: Development of the segregation index in the SIGRT simulation.

and clearer to average them together into a single volume-weighted mean velocity. The averaged 2-D plane is shown in Figs 19 and 20 at six key times which are indicated by circles in Fig. 18. The behavior of the system at these key times is discussed below.

- **15 s**: The instability is developing. The Brazil nut effect is causing large particles to rise to the top. A white layer can be seen at the top of the flow, indicating a nearly pure layer of large particles. Particle flow (in the z-y plane) is noisy, lacking a well-defined large-scale pattern.
- **30 s**: We have reached peak I_s. At this instance we see a larger white layer at the top which has started fingering. For large scale velocity we see the fingers moving downward. This is the (granular) Rayleigh-Taylor instability which looks, at this instant, quite similar to the traditional fluid-fluid RT instability. From here, I_s decreases as the large-particle fingers spill and mix into the mixture below and the competing instabilities are established: the Brazil nut effect drives large particles to the surface and the RT instability pushes them down through the fingers. Large scale recirculation begins.
- **43 s**: Initially there are 4 fingers which merge into three at this instant (two fingers on the right becoming one).
- **53 s**: A local minima of I_s, the surface has become relatively depleted for large particles which begins to recover.
- **90 s**: Near a local maxima of I_s we see another merging event, two fingers (now on the left) are about to merge into one leaving just two.
- **180 s**: The flow is relatively stable over the last minute and a half of the simulation with two large-scale recirculation cells emanating from two RT fingers, supplied by a relatively thin surface layer of large particles.

This simulation was run with `!1245`. However, we note that, somewhat unfortunately, the same general behavior was also observed on `develop` without the tangential history term.

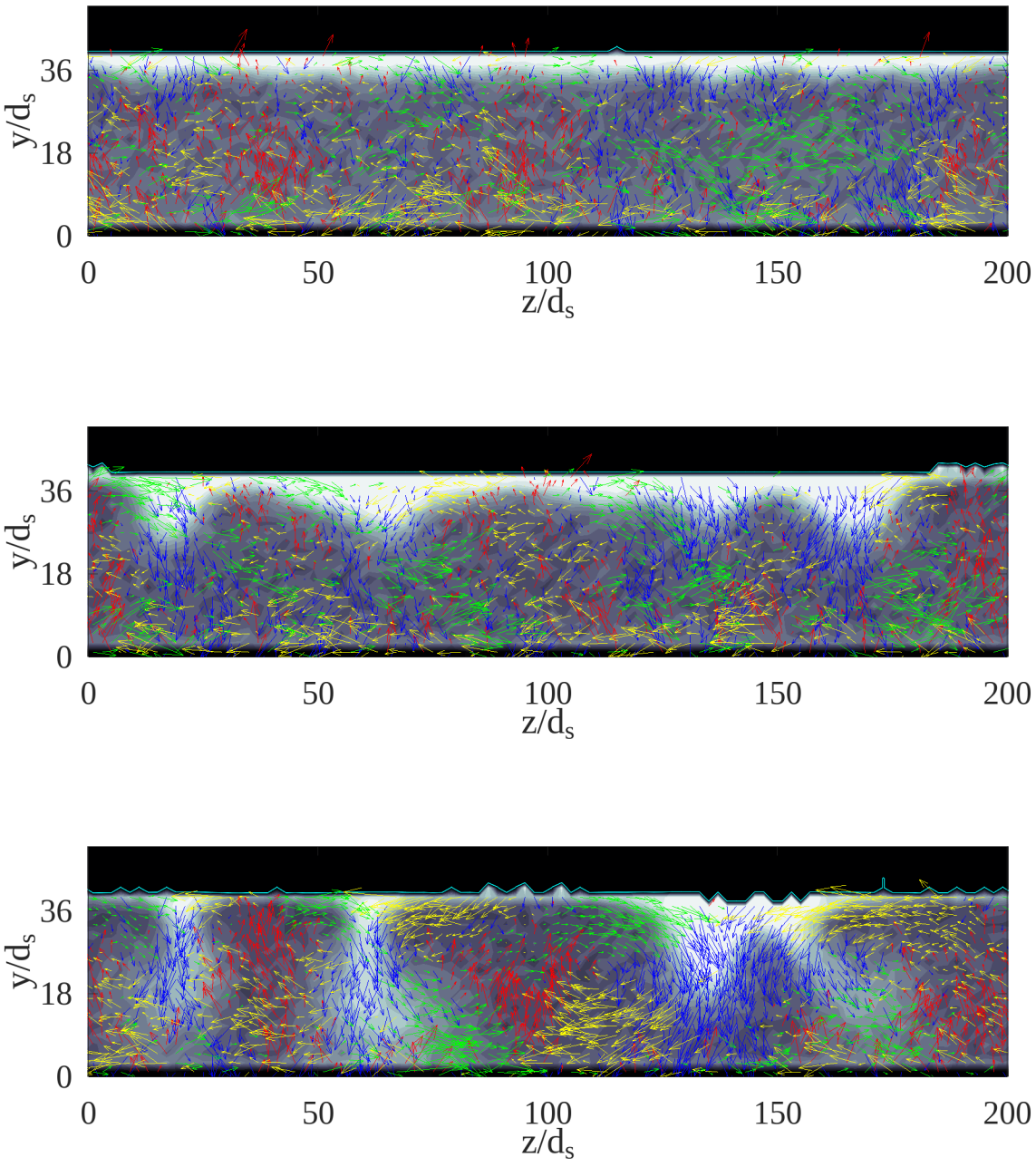

Figure 19: Contour plots of volume-weighted concentration and mean velocity in a 2-D $z - y$ plane at times $t = 15$ s, 30 s, and 43 s (top to bottom). Filled contour shows fraction of particle sizes ranging from entirely small particles (black) to entirely large particles (white). The black region near the top is devoid of particles. To distinguish the void space, the single cyan contour indicates the zero-particle line.

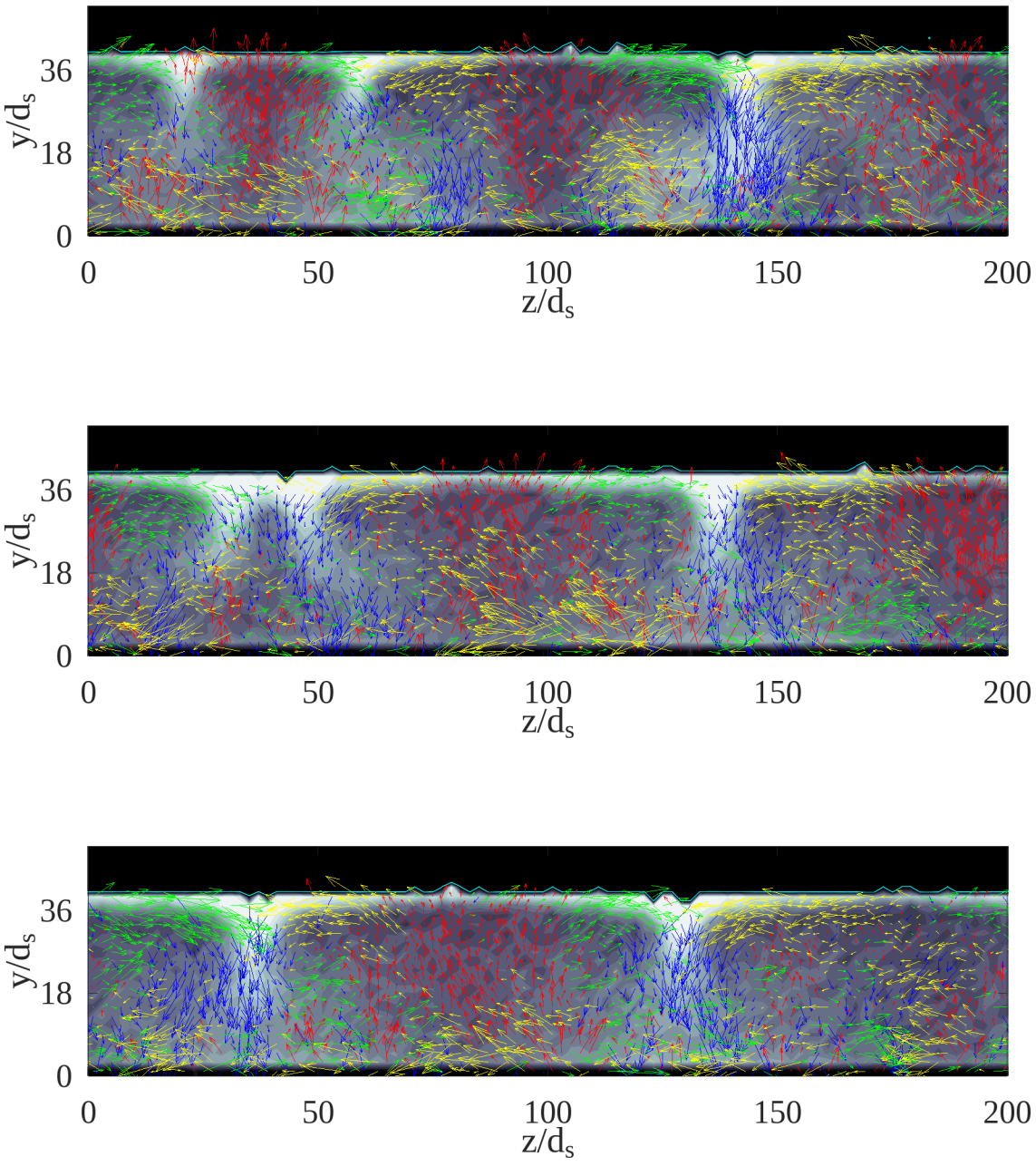

Figure 20: Continuation of Fig. 19 at times $t = 53$ s, 90 s, and 180 s (top to bottom).

Chapter 7: Performance

Before closing, we should discuss the performance of the proposed changes of `!1245`. The current cost of running simulations with tangential history included is two-fold: one is the cost of memory, and the other is the cost of computation. Both costs are directly related to the input parameter `TAN_HIST_MAX_CONTACTS` which sets the maximum number of contacts tracked per particle. The memory increase comes from storing a list of three Reals and two Integers per particle-contact which keeps track of the tangential force and uniquely identifies the contact particle from the previous particle substep. Additionally, there is a temporary list of Bools per particle-contact in each particle substep that accounts for whether a particle-contact can be removed from tracking so that the space can be reused, which happens when colliding particles go out of contact in the current substep. The increase in compute time comes from looking up the appropriate contact from the tangential history particle-contact list so that the force can be added in every particle-neighbor iteration. The performance of the newly implemented model is summarized in Table 8. The performance penalty is the ratio of the time to solution on `!1245` to `develop`. For comparison, we have also included the max contacts setting (i.e. `TAN_HIST_MAX_CONTACTS`) as well as the ratio of largest to smallest particle, $\gamma = \max d_i / \min d_i$, for each case. It is acknowledged that the performance of the current implementation is far from optimal and there are several ways to improve it. For example, improving the speed of lookup from the tangential history particle-contact list through a map-like operation and getting rid of the temporary Bool storage by determining removable contacts through a separate kernel launch up front, are two suggestions for potential performance improvement. Because the performance penalty was not prohibitive for the simulations conducted in this report, it was not investigated in detail. A systematic profiling study to identify the main performance bottlenecks and addressing them is proposed as future work.

Table 8: Performance of the tangential history term as implemented in `!1245` for the cases studied in this work.

case	**penalty**	**max contacts**	γ
constrained pile (center)	1.42	12	1.18
constrained pile (left)	1.31	12	1.18
free pile	1.23	12	1
hopper ($D_o = 0.25$ cm)	1.67	20	1.43
hopper ($D_o = 1.50$ cm)	1.64	20	1.43
SIGRT	3.76	30	2.21

Chapter 8: Conclusions

MFIX-Exa (`https://mfix.netl.doe.gov/mfix-exa`) is a multiphase CFD code primarily targeting particle-laden gas-solid flows. The code was originally developed with large scale simulation in mind; targeting extreme-scale computing from the ground up with the AMReX (`https://github.com/AMReX-Codes/amrex`) HPC software framework provided. As such, MFIX-Exa is a powerful tool for multiphase flow simulation which may extend beyond the originally targeted physics encountered in reacting fluidized systems. This report extends the soft-sphere DEM model so that it may be more applicable to dense granular flows. Additionally, this more complete model may have potential use to simply check assumptions or estimate model form uncertainty in cases that may be well-fluidized in general but be in certain locations or periods of time, e.g., in the L-valve of a CLR [10].

The linear spring dashpot collision model originally developed in MFIX-Exa, i.e., as it appears in the main `develop` branch of the code, neglects a static friction term in the tangential force, see Eq. (10). In other words, the tangential force is always assumed to be the Coulomb limit, see Eq. (12). This simplification is made because, one hand it is not expected to be significant in fluidized systems while, on the other, including the static tangential friction adds complexity and computational expense. Specifically, the linear spring term depends on a tangential overlap that, unlike the normal overlap, can not be directly computed from the instantaneous particle positions. Instead, the tangential overlap must be time-integrated, see Eq. (11),

requiring each particle to store this value *for each other particle* that it is in contact with. Additionally, two common rolling friction models were also investigated in this work.

The collision model is outlined in detail in Section 2. The new collision model, i.e., including static friction term, and the rolling friction models are implemented on a branch of the code which is referred to in this document by its merge request identifier, `!1245`. The new collision model is validated against the single particle oblique collision data of Kharaz et al. [1]. We find good agreement with the data as well as the previous numerical results of Di Renzo and Di Maio [2] for tangential restitution coefficient, rebound angle and rebound angular velocity. Without static tangential friction, i.e., the existing model as implemented in `develop`, the largest resulting error is an under-prediction of the tangential restitution coefficient for small incident angles $0\theta_i < 8°$ (i.e., nearly normal collisions) and an over-prediction for incident angles between approximately $8 < \theta_i < 32°$. There is no change in the prediction for glancing collisions of $\theta_i > 33°$. With the oblique collision test we also do a simple parametric study on some unclosed coefficients of the model. We suggest values of the tangential spring coefficient, $C_k = 0.9$, the tangential dashpot coefficient, $C_\eta = 0.9$, and the time step coefficient $C_\Delta = 32$, which are used in the remainder of the test cases.

Three further test cases are studied: static piles, hopper discharge, and the self-induced granular Rayleigh-Taylor instability (SIGRT). Two different static pile configurations are considered. In the first case, referred to here as a constrained pile, replicates the experiment of Li et al. [3]. The particles are initially contained in a box which rises and the particles are discharged through one of two openings into a second box containing the first. We find that the simplified `develop` model predicts a much lower angle of repose than observed experimentally. Including static tangential friction in the `!1245` model increases the angle of repose, but still under-predicts the data unless the friction coefficient is increased significantly beyond the measured value. Interestingly, neither rolling friction model has an impact on the solution. In the second static pile test, a static bed of particles is also discharged by removing supports. In this case, however, we are interested in the pile that remains on the fixed support rather than the one that forms below the openings. This free pile was studied experimentally and numerically by Zhou et al. [4]. Very much opposite of the constrained pile, we find that tangential force model has no impact on the *long-time* behavior. However, for the free pile, we find that the rolling friction coefficient and model form directly impacts the resulting pile. Good agreement with the experiment is only seen with `ModelA` and $\mu_r \approx 0.01$. The hopper considered here is a cylindrical flat-bottom hopper of diameter $D = 5$ cm which is one of the same originally used by Beverloo et al. [5] to obtain the now famous Beverloo equation, see Eq. (25). The granular media considered is sand. While `develop` shows acceptable agreement with the empirical correlation, `!1245` matches very well. The difference is traced to the solids volume fraction. In the last test, we attempt to reproduce the recently discovered SIGRT instability recently discovered and explained by D'Ortona and Thomas [34]. Though only qualitative, the instability has several unique, defining characteristics that were all faithfully reproduced: initial segregation due to the Brazil nut effect, inverse stratification leading to a Rayleigh-Taylor instability, merging events leading to a stable quasi-steady state similar to a Rayleigh-Bénard instability with counter-rotating vortices.

Finally, the performance of the new model is assessed using the test cases. For monodisperse particles, the slow down is reasonable, only 23% for the free static pile. As the size ratio between the largest and smallest particles, γ increases, the number of possibly colliding neighbors that need to be allocated for each particle must be increased from the suggested default value of 10. For the SIGRT with $\gamma = 2.21$, the max contacts parameter was increased to 30 which resulted in nearly a factor of 4x slowdown.

8.1 Epilogue

The collision model as implemented in `!1245` was merged into the main `develop` branch of the codebase. The model will be made available to users with the `25.04` release. The new input keywords are

```
# enable static tangential friction
dem.tan_history = "true"
dem.tan_history.max_contacts = 20

# enable rolling friction
dem.rolling_friction = "ModelA" #"ModelB"
dem.rolling_friction.coefficient = 1.0e-3
```

References

[1] AH Kharaz, DA Gorham, and AD Salman. An experimental study of the elastic rebound of spheres. *Powder Technology*, 120(3):281–291, 2001.

[2] Alberto Di Renzo and Francesco Paolo Di Maio. Comparison of contact-force models for the simulation of collisions in dem-based granular flow codes. *Chemical Engineering Science*, 59(3):525–541, 2004.

[3] Yanjie Li, Yong Xu, and Colin Thornton. A comparison of discrete element simulations and experiments for 'sandpiles' composed of spherical particles. *Powder Technology*, 160(3):219–228, 2005.

[4] YC Zhou, BD Wright, RY Yang, Bao Hua Xu, and Ai-Bing Yu. Rolling friction in the dynamic simulation of sandpile formation. *Physica A: Statistical Mechanics and its Applications*, 269(2-4):536–553, 1999.

[5] Wim A Beverloo, Hendrik Antonie Leniger, and J Van de Velde. The flow of granular solids through orifices. *Chemical engineering science*, 15(3-4):260–269, 1961.

[6] Weiqun Zhang, Ann Almgren, Vince Beckner, John Bell, Johannes Blaschke, Cy Chan, Marcus Day, Brian Friesen, Kevin Gott, Daniel Graves, Max P. Katz, Andrew Myers, Tan Nguyen, Andrew Nonaka, Michele Rosso, Samuel Williams, and Michael Zingale. Amrex: a framework for block-structured adaptive mesh refinement. *Journal of Open Source Software*, 4(37):1370, 2019.

[7] Weiqun Zhang, Andrew Myers, Kevin Gott, Ann Almgren, and John Bell. Amrex: Block-structured adaptive mesh refinement for multiphysics applications. *The International Journal of High Performance Computing Applications*, 35(6):508–526, 2021.

[8] Douglas Kothe, Stephen Lee, and Irene Qualters. Exascale computing in the united states. *Computing in Science & Engineering*, 21(1):17–29, 2018.

[9] Alexander F., A. Almgren, J. Bell, A. Bhattacharjee, J. Chen, P. Colella, D. Daniel, J. DeSlippe, L. Diachin, E. Draeger, A. Dubey, T. Dunning, T. Evans, I. Foster, M. Francois, T. Germann, M. Gordon, S. Habib, M. Halappanavar, S. Hamilton, W. Hart, Z. Huang, A. Hungerford, D. Kasen, P. R. C. Kent, T. Kolev, D. B. Kothe, A. Kronfeld, Y. Luo, P. Mackenzie, D. McCallen, B. Messer, S. Mniszewski, C. Oehmen, A. Perazzo, D. Perez, D. Richards, W.J. Rider, R. Rieben, K. Roche, A. Siegel, M. Sprague, C. Steefel, R. Stevens, M. Syamlal, M. Taylor, J. Turner, J.-L. Vay, A. F. Voter, T. L. Windus, and K. Yelick. Exascale applications: skin in the game. *Philosophical Transactions of the Royal Society A*, 378(2166):20190056, 2020.

[10] Samuel Bayham, Douglas Straub, and Justin Weber. Operation of a 50-kwth chemical looping combustion test facility under autothermal conditions. *International Journal of Greenhouse Gas Control*, 87:211–220, 2019.

[11] Jordan Musser, Ann S Almgren, William D Fullmer, Oscar Antepara, John B Bell, Johannes Blaschke, Kevin Gott, Andrew Myers, Roberto Porcu, Deepak Rangarajan, Michele Rosso, Weiqun Zhang, and Madhava Syamlal. Mfix-exa: A path toward exascale cfd-dem simulations. *The International Journal of High Performance Computing Applications*, 36(1):40–58, 2022.

[12] J. Capecelatro and O. Desjardins. An euler-lagrange strategy for simulating particle-laden flows. *Journal of Computational Physics*, 238:1–31, 2013.

[13] AB Stevens and CM Hrenya. Comparison of soft-sphere models to measurements of collision properties during normal impacts. *Powder Technology*, 154(2-3):99–109, 2005.

[14] Harald Kruggel-Emden, Erdem Simsek, Stefan Rickelt, Siegmar Wirtz, and Viktor Scherer. Review and extension of normal force models for the discrete element method. *Powder Technology*, 171(3):157–173, 2007.

[15] Peter A Cundall and Otto DL Strack. A discrete numerical model for granular assemblies. *Geotechnique*, 29(1):47–65, 1979.

[16] Y. Tsuji, T. Kawaguchi, and T. Tanaka. Discrete particle simulation of two-dimensional fluidized bed. *Powder Tech.*, 77:79–87, 1993.

[17] NG Deen, M Van Sint Annaland, Martin Anton Van der Hoef, and JAM Kuipers. Review of discrete particle modeling of fluidized beds. *Chemical Engineering Science*, 62(1-2):28–44, 2007.

[18] HP Zhu, ZY Zhou, RY Yang, and AB Yu. Discrete particle simulation of particulate systems: theoretical developments. *Chemical Engineering Science*, 62(13):3378–3396, 2007.

[19] Ciprian T David, Ramon García-Rojo, Hans J Herrmann, and Stefan Luding. Powder flow testing with 2d and 3d biaxial and triaxial simulations. *Particle & Particle Systems Characterization*, 24(1):29–33, 2007.

[20] R. Garg, J. Galvin, T. Li, and S. Pannala. Documentation of open-source MFIX-DEM software for gas-solids flows. Technical report, National Energy Technology Laboratory, Morgantown, WV USA, 2012.

[21] Bruno Blais, David Vidal, Francois Bertrand, Gregory S Patience, and Jamal Chaouki. Experimental methods in chemical engineering: Discrete element method–dem. *The Canadian Journal of Chemical Engineering*, 97(7):1964–1973, 2019.

[22] M.A. van der Hoef, M. Ye, M. van Sint Annaland, A.T. Andrews, S. Sundaresan, and J.A.M. Kuipers. Multiscale modeling of gas-fluidized beds. In Guy B. Marin, editor, *Computational Fluid Dynamics*, volume 31 of *Advances in Chemical Engineering*, pages 65–149. Academic Press, 2006.

[23] H Kruggel-Emden, S Wirtz, and V Scherer. A study on tangential force laws applicable to the discrete element method (dem) for materials with viscoelastic or plastic behavior. *Chemical Engineering Science*, 63(6):1523–1541, 2008.

[24] Christoph Kloss, Christoph Goniva, Alice Hager, Stefan Amberger, and Stefan Pirker. Models, algorithms and validation for opensource dem and cfd–dem. *Progress in Computational Fluid Dynamics, an International Journal*, 12(2-3):140–152, 2012.

[25] Jun Ai, Jian-Fei Chen, J Michael Rotter, and Jin Y Ooi. Assessment of rolling resistance models in discrete element simulations. *Powder Technology*, 206(3):269–282, 2011.

[26] CM Wensrich and André Katterfeld. Rolling friction as a technique for modelling particle shape in dem. *Powder technology*, 217:409–417, 2012.

[27] Kazuyoshi Iwashita and Masanobu Oda. Rolling resistance at contacts in simulation of shear band development by dem. *Journal of engineering mechanics*, 124(3):285–292, 1998.

[28] Leonardo E Silbert, Deniz Ertaş, Gary S Grest, Thomas C Halsey, Dov Levine, and Steven J Plimpton. Granular flow down an inclined plane: Bagnold scaling and rheology. *Physical Review E*, 64(5):051302, 2001.

[29] J Shäfer, S Dippel, and DE Wolf. Force schemes in simulations of granular materials. *Journal de physique I*, 6(1):5–20, 1996.

[30] Roberto Porcu, Jordan Musser, Ann S Almgren, John B Bell, William D Fullmer, and Deepak Rangarajan. Mfix-exa: Cfd-dem simulations of thermodynamics and chemical reactions in multiphase flows. *Chemical Engineering Science*, 273:118614, 2023.

[31] Tingwen Li, Rahul Garg, Janine Galvin, and Sreekanth Pannala. Open-source mfix-dem software for gas-solids flows: Part ii–validation studies. *Powder Technology*, 220:138–150, 2012.

[32] Zekun Wang, Yujun Teng, and Moubin Liu. A semi-resolved CFD–DEM approach for particulate flows with kernel based approximation and hilbert curve based searching strategy. *Journal of Computational Physics*, 384:151–169, 2019.

[33] Kenan Xi, Thomas Kovar, William D Fullmer, Alexander Penn, Jordan Musser, and Christopher M Boyce. Cfd-dem study of bubble properties in a cylindrical fluidized bed of geldart group d particles and comparison with prior mri data. *Powder technology*, 389:75–84, 2021.

[34] Umberto dOrtona and Nathalie Thomas. Self-induced rayleigh-taylor instability in segregating dry granular flows. *Physical Review Letters*, 124(17):178001, 2020.

[35] Song Gao, Julio M Ottino, Paul B Umbanhowar, and Richard M Lueptow. Percolation of a fine particle in static granular beds. *Physical Review E*, 107(1):014903, 2023.

[36] Dhairya R Vyas, Julio M Ottino, Richard M Lueptow, and Paul B Umbanhowar. Improved velocity-verlet algorithm for the discrete element method. *Computer Physics Communications*, page 109524, 2025.

Marianne Walck
Director
National Energy Technology Laboratory
U.S. Department of Energy

David Lyons
Deputy Director & Chief Research Officer
Science & Technology Strategic Plans & Programs
National Energy Technology Laboratory
U.S. Department of Energy

Bryan Morreale
Associate Laboratory Director for Research & Innovation
Research & Innovation Center
National Energy Technology Laboratory
U.S. Department of Energy